Dynamics of binary phase separation in liquid ^{3}He-^{4}He mixtures

James K. Hoffer and Dipen N. Sinha
Los Alamos National Laboratory, University of California, Los Alamos, New Mexico 87545
(Received 16 October 1985)

Binary phase-separation dynamics in liquid mixtures of ^{3}He and ^{4}He has been investigated near the tricritical point with laser-light scattering techniques. Rapid decompression of the mixtures results in quenches into the miscibility gap so that both the metastable and unstable (spinodal) regions can be probed. Quenches into the unstable region allowed measurements of the normalized dynamic structure factor $S(k,t)$ that confirm the dynamical scaling hypotheses for spinodal decomposition. Measurements made for concentrations well away from the tricritical value show different behavior and suggest the presence of a spinodal boundary. Forward scattering intensities for shallow quenches probe nucleation phenomena and permit quantitative measurements of anomolous supercooling as a function of quench rate. Comparisons with data in organic binary mixtures are given.

I. INTRODUCTION

The dynamics of first-order phase transitions is best studied in situations where an intensive thermodynamic variable of a system (e.g., temperature T, pressure P, concentration c, etc.) is suddenly perturbed by a finite amount (ΔT, ΔP, Δc, ...) which causes the crossing of a line of first-order phase transition in the phase diagram. In a typical experiment, a system is rapidly quenched from a disordered equilibrium state to a nonequilibrium state below a phase transition line. The quenched system subsequently undergoes a nonlinear relaxation process to its new equilibrium state, which, in the case of a binary fluid, is the coexistence of two new (ordered) phases. In such experiments, one normally makes a distinction between metastable and unstable nonequilibrium states. From a mean-field theoretical point of view, it is possible to make a sharp distinction between metastable and unstable states. The metastable states are characterized by a positive order parameter and a positive inverse susceptibility while the unstable states belong to the region of the phase diagram below the critical temperature T_c where the inverse susceptibility is negative (see Fig. 1). The two lines that delineate the boundary between metastable and unstable nonequilibrium states below T_c, i.e., the locus of points where the inverse susceptibility vanishes, constitute the classical spinodal curve. Although we shall refer to these two regions separated by the spinodal curves as the metastable and spinodal regions (unstable), it should be recognized that for systems with short-range forces there do not seem to be any sharply defined spinodal curves.[1-4]

The dynamics of the early stage of evolution of a nonequilibrium system toward equilibrium following a quench is different for the two regions. If the system is rapidly quenched from outside the equilibrium coexistence region into the metastable region of the phase diagram, i.e., the region that is considered to be stable with respect to *weak* localized fluctuations, phase separation occurs via nucleation and growth. Small "droplets" or "clusters" of the minority B-rich phase form randomly in the background of the unstable A-rich phase due to thermal fluctuations. Droplets larger than a critical radius R_c grow spontaneously, but droplets smaller than R_c shrink. The rate of formation of these critical-size droplets depends exponentially on the degree of metastability of the system, i.e., on the distance away from the coexistence curve, and the process is described well by homogeneous nucleation theory.[5,6] An explosive increase in the ratio of formation of critical-size droplets effectively determines a kinetic limit of metastability of the nonequilibrium system. The subsequent growth of the droplets beyond the radius R_c to macroscopic domains is limited by diffusive processes and can proceed via several mechanisms, such as Lifshitz-Slyozov[7] evaporation—condensation, droplet coalescence induced by Brownian motion, etc. It is believed that the process of nucleation takes place on a time scale short

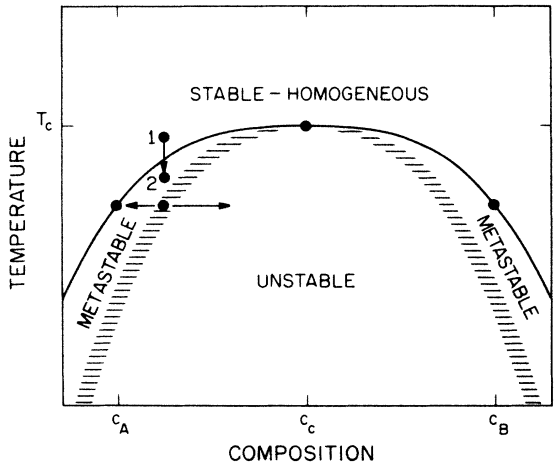

FIG. 1. A miscibility gap in a typical binary system. A thermal quench from point 1 to point 2 leaves the system in a state of metastable equilibrium, where phase separation may proceed by homogeneous nucleation. A deeper quench into the unstable region may result in spinodal decomposition into the two species shown on the coexistence curves. The boundary between metastable and unstable regions is not sharply defined.

compared to the ensuing processes of coalescence and eventual bulk phase separation. It is reasonable to ask whether or not these processes will lead to a more uniform spacing or long-range order of the droplets. If so, then the structure factor $S(k,t)$ of the mixture would develop a peak at a preferential wave vector k_m corresponding to the inverse of the average distance between droplets. One should then observe that light from a coherent beam passing through the mixture is scattered over a finite range of angles, leading to a halolike pattern centered around the primary beam. However, at earlier times during nucleation and ripening, such a light beam would be scattered randomly over all angles up to values corresponding to the shortest average distance between droplets, i.e., the scattering pattern would be that of a diffuse disk. Experimentally, one observes the homogeneous nucleation process when the droplets become numerous enough and large enough to scatter light effectively. This is commonly referred to as "cloud-point" phenomena. Because diffusive processes slow down near the critical point, the droplet growth rate is also accordingly affected. Consequently, in experimental observations of cloud-point phenomena involving finite quench rates, the slowing down of the droplet growth rate near the critical point is manifested as anomalous or larger supercooling than expected from classical nucleation theory. This anomalous supercooling has been observed in widely differing binary liquid systems[8-12] including liquid ^{3}He-^{4}He mixtures.[13]

It is conceptually possible to consider quenches deep into the spinodal region where the system is thought to be unstable with respect to weak delocalized (i.e., long-wavelength) fluctuations of the order parameter. The growth of these fluctuations throughout the entire system into periodic domains (zones) of the two coexisting phases is called the spinodal decomposition mechanism. It should be noted that for quenches into the miscibility gap close to the classical spinodal curve the distinction between the previously described droplet mechanism of phase-separation initiation and long-wavelength instabilities may be less sharp. It has been clearly pointed out by Binder[4] that in such a situation one expects a gradual transition in the dynamics of phase separation as one moves from the metastable to the unstable regions. This gradual transition has been seen in Monte Carlo studies of the evolving structure factor $S(k,t)$. Deep inside the unstable region, nonlinear theories of spinodal decomposition[14] predict that $S(k,t)$ develops a peak at small wave vectors k, which increases in magnitude and whose location $k_m(t)$ moves to smaller and smaller wave vectors with time. Experimentally,[15-22] one observes that a light beam is scattered into a halo pattern which intensifies while collapsing. Monte Carlo simulations of spinodal decomposition in an Ising model[23] have led to a scaling prediction for the normalized structure factor $\bar{S}(k,t)$:

$$\bar{S}(k,t)=[K(t)]^{-3}F(k/K(t)), \quad t \geq t_0 \tag{1}$$

where the "shape" function $F(x)$ is independent of time beyond the "transient" time t_0, and all the time dependence of $\bar{S}(k,t)$ is carried in $K(t)$, where K^{-1} is a measure of the domain size, i.e., $K(t) \propto k_m(t)$.

Spinodal decomposition theory has been invoked to explain the periodic, fine-grain structure of phase domains observed in microphotographs of modern "superalloys."[24] The high mechanical strengths and excellent high-temperature properties of such alloys are thought to be direct consequences of the fine-grain structure. These materials are prepared by very rapid and deep quenching from the melt, e.g., by spraying small molten droplets onto cryogenically cooled surfaces. X-ray scattering studies of such materials show halo patterns, confirming the predicted structure function.

Goldburg *et al.*[25] have discussed why liquid mixtures are more suitable than metallic alloys for studying the dynamic processes of binary phase separation and spinodal decomposition. As a model for such studies, the ^{3}He-^{4}He system has added advantages which include the following: the virtual lack of any possible impurities; the excellent control and uniformity of temperature attainable in initially superfluid states; the ability to propagate temperature changes with velocities of second sound instead of relying on diffusion; the extensive measurements on both pure components and equilibrium mixtures, which afford precise characterizations of initial and final states; and the fact that this system is a direct analog of the Ising-model systems used in Monte Carlo simulation studies.[26] There are, of course, some disadvantages, the least objectional of which is the low-temperature necessary to effect phase separation, $T < 0.867$ K. More troublesome is the rapid speed of the decomposition processes, leading to halo patterns which form and collapse completely within one second. This system also is of tricritical nature, i.e., in addition to the conserved order parameter of concentration, there is a second, nonconserved order parameter in the system, namely the superfluid order parameter, which possibly could complicate the phase-separation dynamics. However, this order parameter has no effect on the refractive index of these mixtures and therefore is, in itself, transparent to optical measurements.

Experimental attempts to quench into the spinodal region are necessarily done at finite speed, and it may be unavoidable that the mixture starts to decompose when the cloud-point region is first reached. Thereafter, during the remainder of the quench, the local concentration values c_A and c_B might tend to follow their respective nucleation cloud curves and veer away from the spinodal region. Therefore, unless there is experimental evidence that clearly distinguishes between spinodal decomposition dynamics and homogeneous nucleation, it may not be possible to prove that the quench actually reached the spinodal region. With this caveat in mind, we present the results of our studies on binary phase separation in liquid mixtures of ^{3}He-^{4}He. In Sec. II we present a brief description of our experimental apparatus. The general aspects of a quench into the miscibility gap following a change in pressure are discussed in Sec. III. In Sec. IV, data on the formation and collapse of halo patterns, formed from states which are either initially homogeneous or initially phase separated, are presented. Section V is concerned with the results of our measurements of nucleation phenomena. Finally, in Sec. VI, we report various visual observations made during the course of our measurements using expanded laser light.

II. APPARATUS AND EXPERIMENTAL PROCEDURES

Our first apparatus, although not of high optical quality, allowed us to make the first visual observations in ^{3}He-^{4}He mixtures of homogeneous binary phase separation, dispersion formation, and collapsing halo patterns in the small-angle forward scattering of light from a laser beam.[16] In order to carry out more precise studies of binary phase separation dynamics, we developed a more elegant optical apparatus, based on our existing ^{3}He single-shot refrigerator insert. We replaced our glass Dewar system with a system of all-metal Dewars and tails fitted with high-quality optical windows. The optical aperture of the Dewar system was approximately $f/2$. The space between the inner vacuum can and the helium can was an extension of the liquid-helium bath. This normally presented no problems because during measurements the helium bath was pumped to well below the λ temperature and exhibited no optical activity. However, we did have to take precautions to prevent air from entering the bath during refilling operations.

A sample cell (cell 2) was built that used a single bellows to compress the mixture by applying external pressure from a regulated ^{4}He supply. This technique avoided a problem observed in the earlier sample cell (cell 1) where the mixtures was compressed directly by a vane pump in the filling line, namely that the composition of the mixture would change noticeably over the course of a day of experimentation. The data taken in this apparatus were sufficiently accurate to show[18] that the ^{3}He-^{4}He system generally obeys the scaling prediction of Eq. (1). The particular design of cell 2, however, produced some experimental difficulties, the most serious of which was the creation of large convection patterns when the mixtures were decompressed, observed by using the laser shadow technique described below. Because such convection would cause the laser beam to probe constantly changing portions of the mixture and also affect the phase-separation dynamics by possibly inducing shear flow that leads to asymmetry in the angular distribution of scattered light,[27,28] we built a third sample cell (cell 3) in which most of the measurements to be discussed here were conducted.

As shown in Fig. 2, cell 3 is equipped with a pair of bellows that work in opposition, resulting in a much more isotropic decompression than could be achieved in cell 2. Laser shadowgraphs showed no noticeable convection patterns following decompression in this cell. To insure that interfaces, if present, would be visible, the cell was designed so that no significant volumes of mixture would be above or below the field of view (shown in Fig. 2 by a dashed circle). The cell windows were made from high-quality optical sapphire to promote temperature uniformity in the mixtures. The high strength of the sapphire helps to avoid chipping and cracking of the windows during the installation with indium seals. The cell was provided with space for sound transducers, as shown schematically in the figure. An ultrasonic transducer, having a reflector supported by thin posts, was installed in the cell during the measurements. However, our measurements of sound velocity and attenuation are still in progress and will not be discussed here.

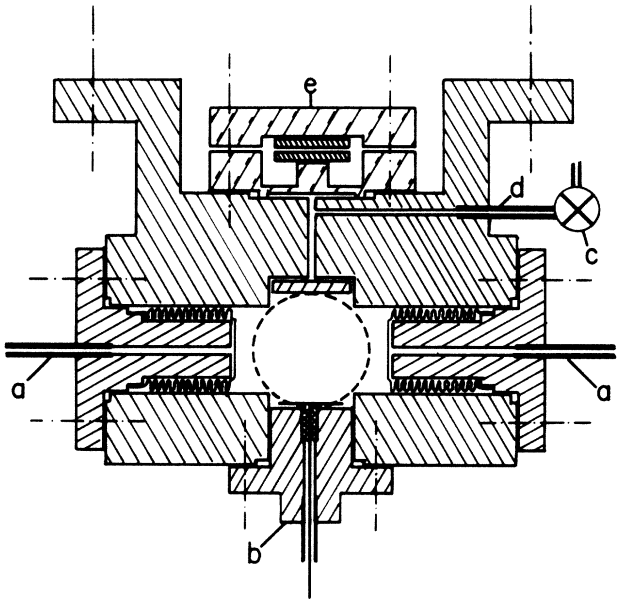

FIG. 2. Schematic of cell 3. The viewable area is indicated by the dashed circle. The ^{4}He lines (*a*) to the two compression bellows are connected to a common line just below the cell. An isolation valve (*c*) is located on the ^{3}He block just above the cell on the fill line (*d*). A capacitive pressure transducer (*e*) monitors the pressure of the ^{3}He-^{4}He mixture in the cell. The cell also contains an ultrasonic transducer (*b*).

Cell temperatures were measured by two germanium thermometers that had been calibrated together against ^{3}He-vapor pressures in previous experiments. One thermometer was greased into a hole drilled into the copper cell body just below one of the bellows cavities, and its leads were anchored to a heater post soldered to the bottom of the cell. Our experience with cell 2, where we have used thermometers both inside and outside the mixture volume, showed that an external thermometer gave an accurate measure of the mixture temperature. The other thermometer was positioned on the ^{3}He platform near a sensitive carbon resistor that was used for thermal regulation. Temperatures were read from separate ac resistance bridges and could be independently regulated from separate controllers.

The *in situ* capacitive pressure gauge (CPG) was calibrated at 1.2 K by first filling the cell and then raising the pressure with a vane pump. Absolute pressures were measured at room temperature with a dial gauge, which itself had been previously calibrated against a dead-weight tester. The capacitance of the CPG was measured to a precision of 3×10^{-4} atm using a General Radio 1615-A capacitance bridge and a lock-in amplifier with a reference frequency of 10 kHz for both drive and receiver. This relatively high frequency was chosen to increase the dynamic response of the measurements. The sensitivity of the CPG was determined to be 0.316 ± 0.003 pF/atm. In the pressure range of 0—4 atm, within which all of our measurements were made, plots of pressure versus capacitance and pressure versus inverse capacitance both showed straight-line behavior. The zero-pressure value of the capacitance ($\sim$30 pF) shifted noticeably after each cool-

down, but the sensitivity was found to be reproducible.

In order to maintain constant mixture composition and to prevent the occurrence of anomalous afterheating following decompression, we placed a pneumatically operated valve in the capillary line, located on the ^{3}He platform. With the valve closed, the measured afterheating agreed with that expected for adiabatic free expansion:

$$(\partial T/\partial P)_S = TV\alpha_P/c_P \ , \tag{2}$$

where V is the molar volume of the mixture, α_P is the isobaric thermal expansion coefficient, and c_P is the heat capacity. There is sufficient thermodynamic data to evaluate this derivative near the tricritical point only for saturated vapor pressures (SVP), yielding a value of -0.0028 K/atm. Our measurements confirm this value and suggest that it does not change significantly up to 2 atm. We employed dc bridge techniques for dynamic cell temperature measurements to verify that the temperature rise did parallel the decreasing pressures up to the fastest rate attainable in our system.

The ^{3}He-^{4}He mixtures were prepared by filling a reference volume with an accurately measured pressure of each pure isotope, followed by pumping the gas into the storage tank where the gases mixed. Small corrections were made to account for the nonideality of the gases, using the second virial coefficients. Subsequent visual observations of the phase-separated liquid interface well below the tricritical temperature T_t confirmed that the composition of the mixtures were accurate to ± 0.0002 mole fraction.

The light source for the scattering experiments was a He-Ne laser ($\lambda = 6328$ Å) with an intensity of 2 mW, beam diameter of 0.63 mm, and a beam divergence of 1.3 mrad. Although the output amplitude showed virtually no noise below 1 kHz and less than 0.5% up to 1 MHz, it was still necessary to spatially filter the beam to reduce spurious scattering. The intensity of the beam was controlled by a variable attenuator and/or by several polarizing plates. A beam steerer was used to position the beam accurately at desired positions near the center of the cell. A 25× beam expander could be inserted into the beam path to provide uniform, parallel, and horizontal light for illuminating the entire visible area of the cell. By placing a diverging lens near the far-side cryostat window, a 30-cm-diam shadow of the cell could be observed on a viewing screen positioned 1.5 m away. We used this method not only to detect interfaces between phase-separated mixtures, but also to make visual observations of the dispersion formation at each new temperature before recording light scattering from the normal (unexpanded) beam. Such observations helped us realize that if the beam were positioned close to the region where the interface eventually would form following phase separation, the resulting halo patterns would develop angular asymmetry at later times during the halo collapse. This asymmetry could be prevented by placing the primary beam slightly away from the location of the ultimate interface. Several other interesting phenomena were observed using this shadow technique, not all of which are fully understood, as discussed in Sec. VI.

The intensity of the small-angle forward scattered light on the far side of the cryostat was measured with a linear self-scanned photodiode array. A complete description of the methods and electronic circuits is given elsewhere[19] and is only summarized here. The array is 2.6 cm long, containing 512 active photodiode elements, each being 12.7 μm wide, 0.43 mm high, and spaced 51 μm apart. For each element there is a storage capacitor to integrate the photocurrent over a variable exposure time, set here to approximately 1 ms to produce the required sensitivity. Circuits purchased with the array read out the voltages on the capacitors at a variable clocked rate, set here to 512 kHz to yield a minimum scan interval of 2.000 ms. We developed special circuitry to block the output of all scans except those at programmable time intervals that were multiples (1—999) of the minimum scan interval, so that a reasonable history of the scattering event could be recorded without overfilling the memory of the digital oscilloscope recorder. Thus, we could record up to eight scans of all 512 angular data points each. We also could block the output of all except every 2^nth element, for n up to 4, and thus record a series of up to 128 scans of 32 elements each, i.e., every 16th element in the array. Of course, the higher number of scans was possible only at the expense of reduced angular resolution, but this feature was useful in previewing a scattering event. It was generally convenient to have at least 16 scans; therefore most of our final data was taken with $n = 2$, i.e., the output from only every other photodiode was recorded.

A thin, back-silvered mirror was placed directly over the photodiode array, having a rectangular area of the silvering removed so that the photodiode elements would be exposed. By placing the assembly at a slight angle to the primary beam, we could deflect the beam without causing large diffraction effects. Even so, the primary beam was typically placed 0.5 to 1.0 mm from the edge of the active elements, sacrificing the lowest-angle data in order to reduce spurious background scattering. The spatial averaging of each element was quite small (each had a small area and the exposure time was short), and because this caused the point-to-point data from the array to be slightly noisy, we introduced passive smoothing by placing a sheet of matte Mylar drafting film directly over the elements, beneath the mirror. The grain size of the matte was much smaller than the diameter of the primary beam, and thus little angular resolution was lost; but the data was much smoother. A single, sensitive photodiode (HUV-1000B, EG&G Electro-Optics) was positioned to intercept the reflected primary beam and thus provide a measure of the transmitted beam intensity $I(0,t)$. The $I(0,t)$ data could be monitored separately from those of the photodiode array and recorded simultaneously with pressure $P(t)$ and temperature $T(t)$ by a fast (100-kHz) multichannel data-acquisition system with 12-bit resolution. In addition, our circuity was designed so that the angular scattering data $I(k,t)$ would be electronically divided by $I(0,t)$ in real time. Therefore, the data were corrected for effects of multiple scattering before being passed on to the digital recorder. Angular data were recorded in terms of the wave vector k, calculated from measurements of the distance between the scattering cell and the photodiode array, the known spacing between active elements ($n \times 51$ μm), the offset of the primary beam

(estimated from the diffuse reflection on the mirror), and the elastic scattering formula $k=(4\pi/\lambda)\sin(\theta/2)$, where θ is the scattering angle.

The data from the digital recorder, $I'=I(k,t)/I(0,t)$, were transferred over an IEEE-488 bus to a Digital Equipment Corporation LSI-11/23 microcomputer, stored on disk during the experiments, and then later retrieved for analysis. The raw data were first corrected for background by subtracting data from one of the "blank" scans recorded before the appearance of the halo pattern. The data were actively smoothed with a three-point moving average algorithm before further processing. As will be discussed in Sec. IV, I' develops multiple peaks at late times in the decomposition. Therefore, instead of analyzing I'_m, the "maximum" scattering intensity, and the corresponding wave number k_m, we computed the first moments I'_1 and k_1 of the data.

For mixtures of tricritical composition X_t at SVP, α_P is positive above 1.025 K, and negative below. The molar volume of the mixture at T_t is equal to the molar volume at approximately 1.2 K. Therefore, we typically began a series of measurements by first cooling the sample cell to 1.2 K before admitting the mixture. This allowed the latent heat of the mixture to be absorbed by the pumped ^{4}He bath (via the heat switch), thus conserving on ^{3}He usage in our single-shot refrigerator. We filled the cell until the liquid-vapor interface was no longer visible, then closed the cryogenic valve by pressurizing the pneumatic line with ^{4}He. The bellows were then prefilled with liquid ^{4}He from a separate supply, again to conserve ^{3}He. The heat switch was then opened and the cell was cooled to the regions of interest. In this manner, we could be assured that we have not overfilled the cell, and therefore that we could make measurements at SVP. The CPG served to confirm that the pressures did not exceed SVP.

We could quench the mixture into the miscibility gap by first pressurizing the bellows, then opening a fast-acting solenoid valve in the bellows system leading to a vacuum pump. Such a quench, from high pressure to SVP, is desirable because the final state is well characterized thermodynamically. However, due to the high compressibility of ^{3}He-^{4}He mixtures near SVP and due to the finite volume of the vacuum system, the rate of decompression is slow and the pressure does not follow an exponential decay. We chose to work around this problem by quenching only to near 0.65 atm. This was easily accomplished: instead of venting the ^{4}He charge in the pressurization bellows to a vacuum pump, we merely vented to the atmosphere. Atmospheric pressure at our laboratory is $\sim$0.76 atm. Subtracting the small force needed to extend the bellows, the resulting pressure P_f in the mixture was 0.65 ± 0.03 atm, depending on how much the cell was underfilled initially. By using the largest bellows supply lines which did not produce excessive heat leaks to the ^{3}He-cooled system, we achieved a decompression rate of nearly 7 atm/s when venting the bellows to the atmosphere. As measured with the CPG and our data-acquisition system, the pressure decay accurately fit an exponential curve with a time constant of 0.075 s. The tricritical composition X_t is also a function of pressure, and it was necessary to increase the ^{4}He concentration of our mixture by $\sim$0.006 mole fraction to maintain the tricritical composition of the equilibrium (low-pressure) state. We verified the composition of the mixture at SVP by cooling the sample in small steps until we first noted the appearance of a phase-separation interface. The pressure was then increased to atmospheric where the tricritical nature of the composition could be checked more sensitively during cooling. If the composition was slightly ^{3}He rich relative to the tricritical composition $X_t(P_f)$, the interface appeared sharply at the bottom of the cell, rising upwards as the temperature was lowered further. But when the mixture was slightly ^{4}He rich, the observations were complicated by the appearance of the gravity-induced superfluid-normal interface, as discussed in Sec. VI. Nonetheless, our observations confirmed that the composition of our mixture was typically within ±0.001 mole fraction of $X_t(P_t)$, which is comparable to the experimental uncertainty in the location of the tricritical line $T_t(P)$ versus $X_t(P)$.

We cooled the cell to the desired initial temperature T_i and regulated the temperature by one of two temperature regulators. If we planned to measure the temperature rise following decompression, then we would regulate the temperature of the ^{3}He platform and monitor the thermometer located on the cell body. We could obtain slightly better temperature stability in the cell, i.e., ±50 versus ±75 μK, by regulating the cell thermometer-heater and letting the ^{3}He-pot "float." After we had determined that the temperature rise was in fact accurately given by Eq. (2), we used only the cell regulator, in spite of the fact that this resulted in a small vertical temperature gradient over the cell. By switching between the two regulators, we determined that the maximum temperature gradient caused by the use of the lower regulator alone was 0.1 mK/cm. Actually, we cannot be certain that the use of the upper regulator alone did not lead to vertical temperature gradients, because the total measured temperature difference of 0.6 mK was within the accuracy of our intercalibration.

We compressed the mixture to the desired initial pressure P_i by admitting more ^{4}He to the bellows from the room-temperature gas regulator. Equilibration, as noted on a chart recording of the CPG bridge output, took 5–15 min, depending on how close we were to the tricritical temperature. The solenoid valve in the bellows supply line was closed and the supply side of the system was vented to the atmosphere. The selenoid valve was then opened, causing the mixture to decompress. A special circuit had been built so that opening the valve caused a trigger signal to be sent to the data-acquisition system. The same trigger signal activated the photodiode array circuitry that, in turn, triggered the digital recorder after an adjustable preset delay period. Direct venting of the bellows resulted in the fastest decompression rate, as noted above. However, the decompression could be made to proceed more slowly by valving the bellows supply line into one of three different series impedances, resulting in additional decompression rates of approximately 2.2, 0.9, and 0.4 atm/s. These are average values for the initial decompression rates and they depend slightly on the initial pressure differential.

III. GENERAL ASPECTS OF PHASE SEPARATION IN ^{3}He-^{4}He MIXTURES

A. Pressure quenches in a system having an asymmetric phase diagram

Before presenting the details of the light scattering data, we wish to comment on several aspects of phase separation in the ^{3}He-^{4}He system and, specifically, on the effect of asymmetry in the phase diagram on a pressure-induced quench into the miscibility gap. Consider Fig. 3, which shows the relevant portion of the concentration-temperature (X-T) phase diagram at several pressures in the range of our experiments. It is obvious that a modest pressure change significantly displaces the phase boundaries, making a pressure-induced quench feasible. We shall consider the final equilibrium state to be at a pressure $P_f = 0.65$ atm (the temperatures and concentrations shown in Fig. 3 are shown relative to the tricritical X,T values for P_f). The point labeled A' represents an initial state where the (relative) temperature is -0.01 K, the (relative) concentration is 0.0, and the pressure P_i is 1.0 atm above the final value. This state is homogeneous because it lies above the phase separation boundary for P_i. Incidentally, this state is also superfluid. If the pressure were suddenly decreased to P_f, the state first shifts from A' to the point labeled B, due to the adiabatic heat of free expansion discussed in the previous section. With respect to the phase boundaries at P_f, state B is unstable and will decompose, leading to two new states. At equilibrium, $\sim 82\%$ of the mass of the mixture will be in the ^{3}He-rich state labeled B_3, and the remaining 18% will be in the heavier, ^{4}He-rich state labeled B_4. The pressure-induced quench from A' to B can be viewed as equivalent to a temperature quench from the state labeled A to the state B, where A is now considered the "initial" state with respect to the phase boundaries for P_f, i.e., A is related to the P_f phase boundaries as A' is related to the P_i boundaries. Note, however, that this quench is no longer vertical, i.e., there is also a shift in the relative concentration because the line A-B must closely parallel the tricritical line $X_t(P), T_t(P)$. (It would be exactly parallel in the absence of free expansion heating.) Although both X_t and T_t are nonlinear functions[29,30] of P, the relationship between $X_t(P)$ versus $T_t(P)$ is surprisingly linear from SVP to 3 atm. The entire tricritical line, from SVP to the freezing pressure, can be fitted to within 0.003 mole fraction by a simple two-term equation:

$$X_t(P) - X_t(\mathrm{SVP}) = 0.303\,712\,4\Delta - 4.412\,25 \times 10^6 \Delta^9 , \quad (3)$$

where $\Delta = T_t(\mathrm{SVP}) - T_t(P)$. The line A-B crosses the P_f phase boundary on the superfluid side, and therefore this cannot be considered a critical quench in the conventional sense, even though the final state is of tricritical composition. In other words, the quench does not enter the spinodal region directly by crossing the tricritical point, but crosses the metastable region first. This illustrates the general difficulty in producing tricritical quenches in a system with an asymmetric phase diagram using a pressure quench technique, namely, in order to quench to varying equivalent temperature depths and have each quench line pass directly through the tricritical point, one would have to prepare a mixture of different composition for each initial temperature and carefully control each initial pressure.

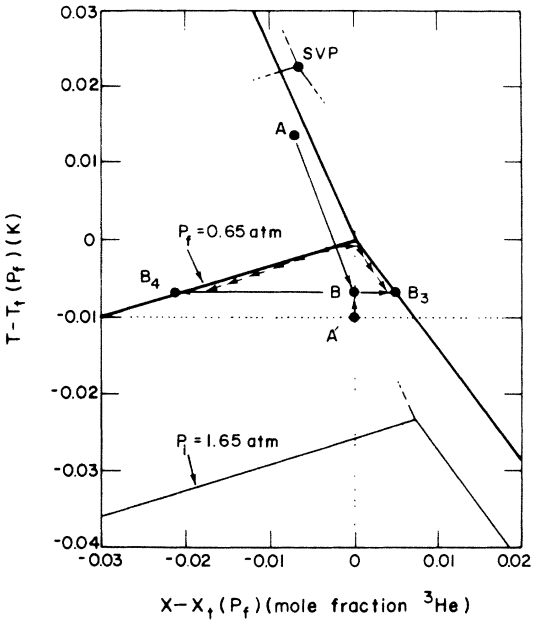

FIG. 3. Phase diagram and idealized decomposition paths for a pressure-induced quench in a ^{3}He-^{4}He mixture of tricritical composition. The state labeled A' is homogeneous at the initial pressure P_i and is of tricritical composition with respect to the final pressure P_f. The heat of adiabatic decompression raises the temperature to the point labeled B. The equivalent temperature quench with reference to P_f is shown by the path $A \rightarrow B$. A rapid quench to the state B would induce spinodal decomposition into the two new states B_3 and B_4. A slow quench would allow homogeneous nucleation and the emerging states might follow the classical cloud-line paths shown by the short arrows.

For a mixture of tricritical composition, all possible final states in the P_f phase diagram can be accessed by allowing the initial state to be already phase separated, as shown in Fig. 4. Here, the initial (relative) temperature is -0.03 K and the mixture is phase separated, ~ 45–55% by mass, into the states labeled C' and E'. Assuming the heat of free expansion to be the same for these states, a sudden decompression carries C' to the point labeled D and E' to the point labeled F. Again, the quench may be considered in reference to the P_f phase diagram only, where two simultaneous independent quenches occur, namely $C \rightarrow D$ in the lower initial phase and $E \rightarrow F$ in the upper initial phase. The state F is unstable and must decompose into two phases, only one of which, labeled F_3, can be shown in the figure. By mass, the fractions of resulting phases F_3 and F_4 are $\sim 93\%$ and 7%, respectively. State D is also unstable and must decompose to the same two states, F_3 and F_4, but now with mass fractions 68% and 32%, respectively. The final equilibrium state,

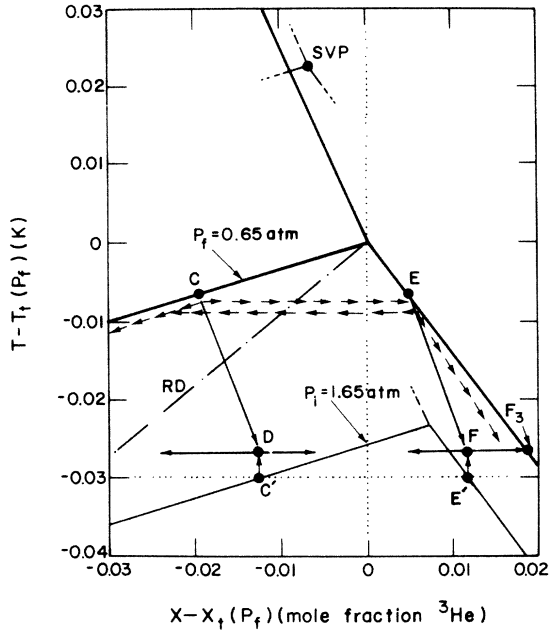

FIG. 4. Phase diagram showing idealized off-tricritical quenches. When the initial, pressurized, state is already phase separated, decompression results in two independent binary phase-separation processes. As described in the text, the interface initially present between the two separated phases vanishes as the decomposition processes proceed.

after gravity has settled the two dispersions, again will be a 82—18 % mixture of upper ^{3}He-rich phase F_3 and lower ^{4}He-rich phase F_4, respectively. Note that both the dispersions formed in the upper and lower initial phases are qualitatively similar, i.e., both ultimately form a dispersed state of ^{4}He-rich droplets (F_4) in a background of continuous ^{3}He-rich phase (F_3). This is because both states D and F lie well to the right of the rectilinear diameter (RD) (shown as a dot-dashed line) of the P_f phase diagram. Consequentially, the interface present between the initial upper and lower states C' and E' (or C and E) must vanish in the same time scale as the formation of the dispersions. Using our shadow techniques, we have verified that this does occur: the interface appears to vanish rapidly following the decompression and the only delineation between the two original phases is the higher fraction of the minor phase F_4 that forms in the lower state (32% versus 7%). The upper dispersion formed from the decomposition of state F proceeds by the continual formation of ^{4}He droplets from the metastable ^{3}He-rich "mother phase," until the composition of this background phase is so depleted in ^{4}He that it reaches F_3. However, the state D undergoes a quite different metamorphosis. Consider the quench to D as being along the path $C \rightarrow D$. As the quench proceeds, the system first reaches the superfluid-side cloud region. Therefore, ^{3}He-rich droplets first evolve from the metastable ^{4}He-rich superfluid. The fraction of the system in the ^{3}He-rich dispersion reaches 50% when the quench line C-D crosses the RD. The ^{3}He-rich droplets then no longer can be considered as the minor phase. It is probable that a percolating structure of ^{3}He-rich phase develops prior to this (when the volume fraction of ^{3}He-rich phase reaches ~20%), and this structure ultimately consumes 68% of the total mass, leading to the formation of a ^{4}He-rich minor phase, either in the form of isolated, dispersed droplets, or as another percolation substructure. Note that the quench $A \rightarrow B$ in Fig. 3 must also follow a similar evolution, as must all such homogeneous, tricritical-type quenches. Therefore, dispersions formed from quenches of the type $A \rightarrow B$ or $C \rightarrow D$ may be considered as proceeding by the continual formation of ^{3}He-rich phase from the metastable ^{4}He-rich mother phase, until the composition of the mother phase is so depleted in ^{3}He that it reaches F_4, by which time it is a fragmented, minor phase.

We are able to study the evolution of such dispersions because of the development of halo patterns in the small-angle scattered light, as shown in Fig. 5. These patterns were recorded following a quench of the type $A \rightarrow B$ using a high-speed camera running at 50 frames/s. The camera

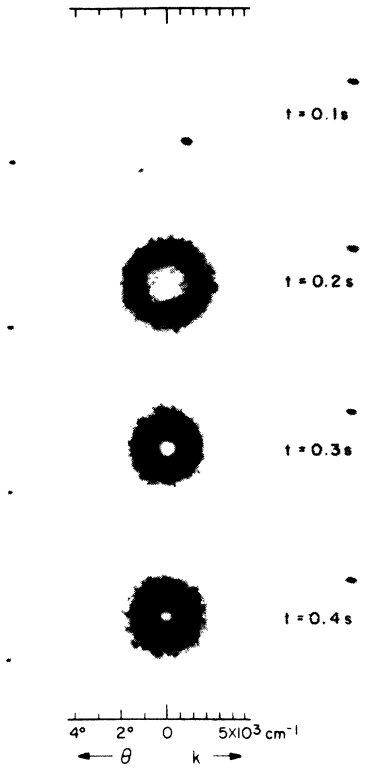

FIG. 5. Halo patterns in the light scattered by a liquid binary mixture of ^{3}He-^{4}He, following a pressure quench from 1.36 atm to the SVP at a temperature of 0.83 K. The mixture is of tricritical composition relative to the SVP phase diagram. The rate of decompression was approximately 0.68 atm/s during the events shown here. These are selected frames from cinematography shot at 50 frames/s, of the image formed by the scattered light on a viewing screen. The primary laser beam is allowed to pass through a 7-mm-diam hole, just visible only in the frame at 0.4 s. The three stationary black dots are the result of reflections of the primary beam from any of the ten optical windows along the light path in our cryostat.

actually recorded the patterns on a viewing screen placed 1.5 m from the scattering cell. A 7-mm-diam hole had been punched in the screen to allow the primary laser beam to pass through. No special film was needed; the images were vividly apparent to the naked eye in the darkened room. We frequently made us of such simple visual observations of halo patterns before recording them with our photodiode array. However, quenches of the type $E \rightarrow F$ generally do not lead to visible halo patterns. Instead, what is typically observed is a very weak, diffuse, collapsing disk of scattered light, more reminiscent of what would be expected from homogeneous nucleation of the minor phase. Such scattering patterns are visible to the naked eye on our viewing screen if the room is well darkened, but the intensities are not sufficient to permit recording by our linear photodiode arrays. Therefore, all of the quenches to be discussed in this paper are of the type $A \rightarrow B$ or $C \rightarrow D$, i.e., the mixture is either initially homogeneous at composition $X_t(P_f)$ or the laser beam is positioned in the lower phase of an already phase-separated mixture at P_i.

B. The effects of a finite rate of quench

In a previous publication,[17] we reported the slowing down of the halo collapse rate as the tricritical point is approached. Here, we report our observations of the dependence of the halo collapse rate on the rate of decompression. As explained in Ref. 17, for these purposes the halo collapse rate can be estimated from the time interval t_k measured between the onset of light scattering [from the $I(0,t)$ signal] and the time when the value k_1 has fallen to a fixed value, taken here as 4000 cm^{-1}. In terms of the equivalent temperature quench, the decompression rates given in Sec. II are 200, 67, 27, and 12 mK/s, respectively. In general, regardless of the coordinate X,T in the P_f phase diagram where phase separation is assumed to begin and regardless of whether the mixture is initially homogeneous or phase separated, we find that the halo collapse rate slows down with lower quench rates as shown in Fig. 6. We have observed that the light scattering history of a given decomposition is qualitatively similar regardless of the quench rate. Figure 7 shows data for $P(t)$, the transmitted light intensity $I(0,t)$, and $I_s(13°,t)$, the scattered light intensity monitored separately at a fixed angle $\theta = 13°$, measured simultaneously for a quench of the type $C \rightarrow D$ at two different quench rates of 67 mK/s [Fig. 7(a)] and 12 mK/s [Fig. 7(b)]. Note that the time scales for the two figures differ by a factor of 4. The initial and final temperatures and pressures are identical for both quenches. For each quench, a slight kink in the $I(0,t)$ data indicates the onset of light scattering and is taken as the origin of the time scale for the decomposition. Note that this occurs at roughly the same pressure for each quench rate, indicating that light scattering begins when the cloud region is reached. The dashed vertical line indicates the instant the photodiode array begins recording the angular scattering $I'(k,t)$ following the preset delay period. The vertical arrows show the times when the peak in the $I'(k,t)$ data reaches various values of k, and demonstrate the collapse of the halo pattern. The value 10×10^3 cm^{-1} corresponds to the k value at the far edge of the array where the peak in $I'(k,t)$ is first detected.

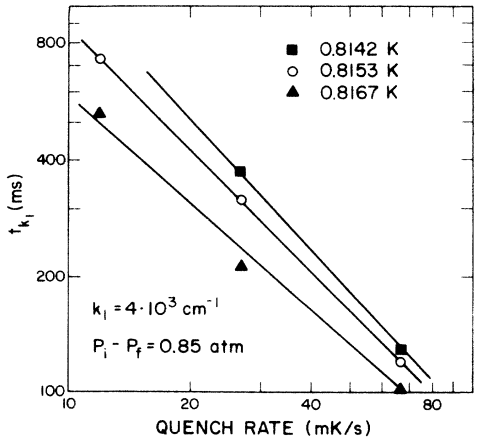

FIG. 6. Halo pattern collapse rate as a function of the equivalent temperature-quench rate. Note that at each quench rate, the data show anomalous "speeding up."

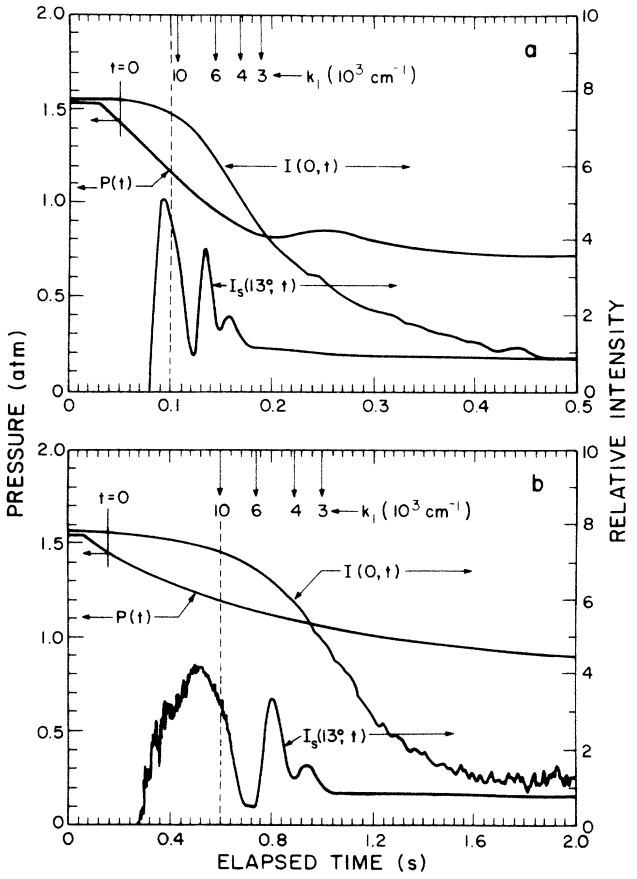

FIG. 7. Quench histories using two different rates of decompression, starting from identical initial conditions. The initial temperature is 0.8153 K and the mixture is initially phase separated as in Fig. 4. See text for more details. At the lower quench rate, the wide-angle scattering is quite noisy, suggesting that homogeneous nucleation plays a role in the initiation of phase separation.

[The hump in the $P(t)$ data in Fig. 7(a) is an anomaly that we observe only when quenching at this particular rate, most likely due to a sonic reflection in the decompression line. The effect of this pressure surge on the light scattering data is of little significance because it occurs after the halo pattern has collapsed to low wave vectors.] For these initial conditions, the dynamics are quite rapid because the temperature is significantly lower than $T_t(P_f)$ and the rates are only minimally affected by tricritical slowing-down phenomena. Note in Fig. 7(a) that the photodiode array follows the halo pattern to an almost complete collapse in less than 0.2 s. If we had used the 200 mK/s quench rate, our data acquisition would not have been rapid enough to accurately follow the phase-separation dynamics. Because a sizable increase in the sensitivity of our method is possible by choosing not to quench at the fastest possible rates, most of the studies reported here were not done with the fastest possible quench rate. However, we typically used the fastest rate consistent with the limitations imposed by our data-acquisition system. Thus, we cannot refute the conjecture that in liquid mixtures binary phase separation on a microscopic scale take place so rapidly that the observed effect of collapsing halos in the scattering pattern is merely a manifestation of the growth of domains or clusters of near-equilibrium-concentration minor phase. This line of reasoning also has been expressed by Alpern *et al.*[31]

C. Precursors to the collapsing halo patterns

There is a considerable period of time between when light scattering first occurs [as observed by the kink in $I(0,t)$] and when the photodiode array first senses light scattered at its extermity, as seen in Fig. 7. To study where this "missing" light goes, we have on occasion placed a sensitive photodetector, identical to the one used to measure $I(0,t)$, at wide scattering angles from the primary beam. The signal, $I_s(\theta,t)$, was amplified by a factor of 100 using a PAR-113 preamplifier and recorded along with $P(t)$ and $I(0,t)$. Surprisingly, we typically see more than one peak in $I_s(\theta,t)$ as shown in Fig. 7 for $\theta=13°$ ($k\sim 2.2\times 10^4$ cm^{-1}). The first peak in I_s is interpreted as the precursor to the halo pattern seen immediately afterwards by our photodiode array. However, the origin of the following peaks is not completely understood at the present time. We have ascertained that the first peak occurs out to the largest angles permitted by our optical cryostat, approximately 25° ($k\sim 4.3\times 10^4$), where it is just barely detectable. By reproducing a given quench and measuring at different angles each time, we find that the first observed scattered light appears to begin nearly simultaneously at all angles greater than approximately 10° (see Fig. 8), while the first peak subsequently shows a growth in intensity and a collapse in wave vector consistent with that measured by the photodiode array. Figure 8 shows that the first detected scattered light tends to level off at a finite delay time, but this is an artifact of the system. The single photodiode at wide angle probes a relatively small portion of the total scattering volume and does not detect anything below a given threshold. However, the photodiode recording $I(0,t)$, while having the same

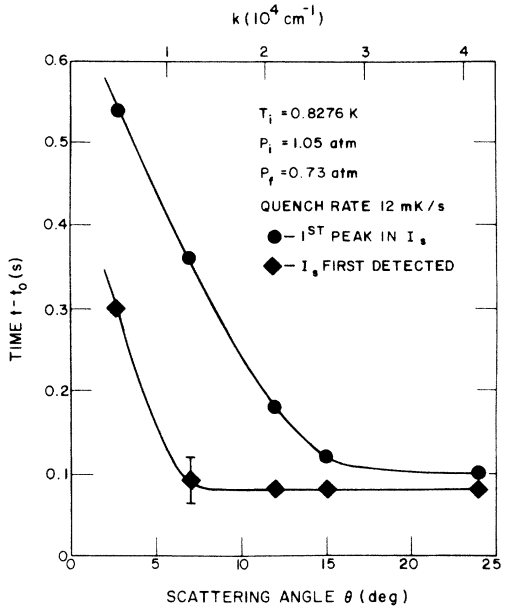

FIG. 8. Time delays to the first detection of scattered light and to the first observed peak in scattering intensity at wide angles. These were measured using a single, sensitive photodiode.

sensitivity, probes the total scattering volume as noted by a decrease in intensity. Therefore the initial decrease (defining $t=0$) is apparent before light at wider angles is first detected. We have not made enough measurements of the second and third peaks in I_s to determine whether they represent collapsing halos. (Note that in using a single fixed photodiode to record a peak in light intensity that is changing spatially, one cannot determine the absolute direction of motion.) When the initial temperature T_i is close to $T_t(P_f)$, we typically observe only two peaks in I_s ($\theta\sim 15°$), the second being only somewhat smaller in magnitude. At slightly lower values of T_i, three peaks appear, as shown in Fig. 7. At still lower temperatures, the second peak becomes larger than the first and the third becomes somewhat noisy. At the lowest temperatures, the third peak is very noisy and larger in magnitude than either the first or the second peak, while occasionally a weak fourth peak is evident. These interesting effects clearly warrant further study.

IV. THE FORMATION AND COLLAPSE OF HALO PATTERNS IN THE SCATTERED LASER LIGHT— THE DYNAMIC STRUCTURE FACTOR

A. Tricritical and near-tricritical quenches

Angular light scattering data recorded during a typical quench of the type shown in Fig. 3 are presented in Figs. 9 and 10. In these measurements, the initial pressure was 1.145 atm and the initial temperature was 0.8290 K. Under these conditions, the initial state of the mixture lies just below the phase-separation line and, consequently, the concentration of the lower portion of the mixture is slightly affected. The data presented are already corrected

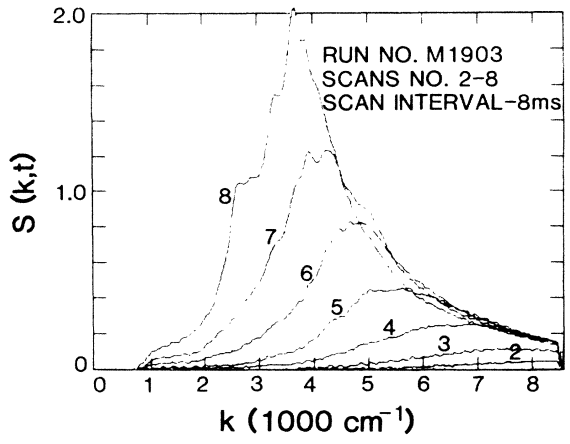

FIG. 9. Light scattering intensity (structure factor) vs scattering angle (wave vector) for the earlier time scans during a quench of the type A-B shown in Fig. 3.

for multiple scattering as discussed in Sec. II. The first photodiode array scan was essentially flat at all but the lowest k values and was used to correct for background scattering. Scans 2—8, taken at 8-ms intervals, are shown in Fig. 9. The data at earlier times show a smooth evolution of a broad peak in the $S(k,t)$ that intensifies while collapsing to lower wave numbers. The data for scans 2—5 or 6 should provide a good test of the scaling hypothesis as represented by Eq. (1). However, at later times, there is strong evidence for the development of substructure in the angular scattering. This is even more pronounced in Fig. 10, where all the recorded scans for the same quench are shown except for scan 2 and scans 15 and 16 (which show clipping due to signal levels too high for the input range of the recording oscilloscope). The existence of the substructure will obviously cause problems in attempts to scale the data at later times. While the substructure is not well understood at the present time, it is worth pointing out a few features. The substructure is absent at earlier times, which rules out the possibility of its being caused by optical imperfections in the light path

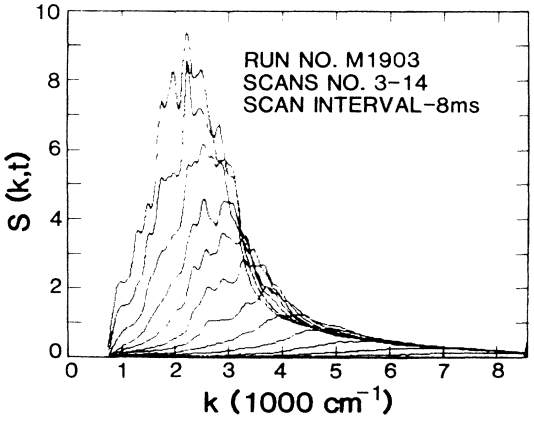

FIG. 10. Later time scans for the quench shown in Fig. 9. Substructure develops during the later time scans, as discussed in the text.

and, similarly, also tends to rule out the possibility of "laser speckle." Furthermore, the periodicity of the substructure is not consistent with what would be expected from Mie scattering for the droplet size distribution derived from the k values. The substructure persists for many scans, each subpeak growing at a virtually constant value of k and subsequently collapsing. Actually, there is a slight shift of each subpeak with time, but this is consistent with the continually changing density of the quenching mixture. From this data, which is typically of all of the quenches we have measured in cell 3, one would tend to conclude that the growth of the main peak in $S(k,t)$ evolves by a growth of subpeaks of successively lower values of k, such as might be due to the coalescence of droplets having a narrow initial size distribution. An analysis of the k values of successive subpeaks based on a monodisperse set of droplets coalescing into doublets, triplets, etc., give results which were consistent with the measured values only within ±25%, and is therefore suggestive but not conclusive. Remembering that the overall halo patterns (see Fig. 5) are not smooth, but an assembly of finite spots, we can probably identify each subpeak with a given spot. There was also some evidence in our latest high-speed photographic measurements that spots grew in intensity at fixed positions from frame to frame. But what we find most remarkable is the reproducibility of the substructure. In Fig. 11, we show an averaged set of data from four separate quenches, all at the same initial conditions. (The initial temperature is nearly identical to quench M1903 shown in Figs. 9 and 10. The photodiode array was positioned farther away, allowing slightly better angular resolution and permitting data collection to lower k values, hence the longer scan interval.) The data from all four quenches were averaged point-to-point, resulting in 4096 data points, each of which was an averaged value of the four different quenches. The first 256 points, representing the averaged first time scan, were used for background subtraction, following the usual three-point smoothing operation. If the substructure seen in each

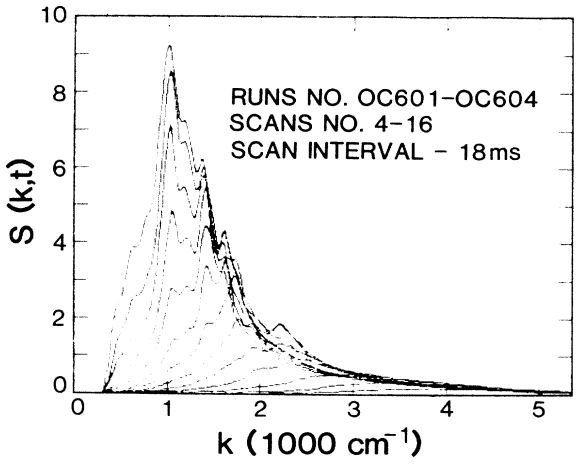

FIG. 11. Averaged light scattering intensity vs wave number. The data from four independent quenches, all performed under identical conditions, have been averaged to produce one set of time scans. Note the persistence of the substructure.

quench were random, we would expect to see roughly four times as many subpeaks in each of the averaged scans, and subpeak heights which were less prominent. In other words, averaging should have led to smoother data. Instead, there is no apparent difference between data from the individual quenches and the averaged data. We should mention that not every one of the four data sets showed the exact same substructure. Often, one or two of the subpeaks would be absent from a given quench. However, for each of the four quenches, there were no subpeaks at positions intermediate to those shown in Fig. 11.

Because the magnitude of the substructure is typically less than $\pm 10\%$ of the overall $S(k,t)$ value, we have proceeded with a scaling analysis of the data. It should be noted that the subpeaks which are in registry in Figs. 9 and 10 will not necessarily be in registry in a scaled plot. This is because the scaling parameter k_1 is largely independent of the presence of substructure.

Following the analysis presented by Craievich and Sanchez,[32] we evaluate our data by first calculating the unnormalized nth moments of the structure function, defined by

$$S_n(t)=\int_{k=0}^{k=\infty} k^n S(k,t)dk \ , \tag{4}$$

and the normalized moments

$$k_n(t)=S_n(t)/S_0(t) \ . \tag{5}$$

As is obvious from Fig. 9, the calculations of $k_n(t)$ for the later time scans are only slightly in error due to the finite range of the measured k values. However, for the earlier time scans, the moments would be in serious error and would lead to a leveling off of $k_1(t)$ at $t=0$, as we have reported previously.[16] To eliminate this artifact, each time scan $S(k,t)$ versus k was fit to a modified Lorentizan function for the purpose of extrapolating the data both to higher k values and to $k=0$, permitting a consistent evaluation of the $S_n(t)$ values by summing $k^n S(k,t)$ from $k=0$ to $3k_1$ for n values of 0, 1, and 2:

$$S_n(t)=\sum_{k=0}^{k=3k_1} k^n S(k,t) \ . \tag{6}$$

We emphasize that the fitting parameters are used only to generate extrapolated data for use in summing Eq. (6). The actual data points, at equal intervals of k, are used over the measured range of k. The moments calculated for quench M1903 (Figs. 9 and 10) are shown in Table I.

As a consequence of the scaling hypothesis,[23,32]

$$S_n(t) \propto [K(t)]^{n-2} \tag{7}$$

and

$$k_n \propto [K(t)]^n \ , \tag{8}$$

where K^{-1} is a measure of the time-dependent domain size. Therefore, one expects the ratios S_0/S_1^2 and k_2/k_1^2 to be constants. These two ratios are related by S_2, the total integrated scattering intensity:

$$S_0/S_1^2=(1/S_2)(k_2/k_1^2) \ . \tag{9}$$

However, the total integrated scattering intensity contains a factor proportional to $(\Delta X)^2$, where ΔX is the difference between the concentrations of the evolving species.[33,34] In our system, where the dynamics of phase separation proceeds on a time scale equivalent to the quenching speed, this is clearly not a constant. This explains why the values for S_2 and S_0/S_1^2 in Table I are changing with time. It also explains why our unnormalized data do not follow the scaling prediction [Eq. (1)], whereas unnormalized data from other experiments in slower systems[35] where the quenching techniques are relatively instantaneous, do appear to scale.

Note, however, that the ratio of normalized moments k_2/k_1^2 is reasonably independent of time. (The slight departure for scans 13–16 appears to be due to the development of a large subpeak.) This suggests that the normalized $\bar{S}(k,t)$ data, i.e., $\bar{S}(k,t)\equiv S(k,t)/S_2(t)$, should scale as predicted by Eq. (1). This scaling is illustrated in Fig. 12. The data for scans 2 and 3, which have a rela-

TABLE I. Time evolution of the moments of the dynamic structure factor in a ^{3}He-^{4}He mixture.

Scan	t (ms)	S_2 (10^{13})	S_0/S_1^2 (10^{-14})	k_1 (cm^{-1})	k_2/k_1^2
2	28	1.217	9.696	10616	1.180
3	36	2.434	4.846	9352	1.179
4	44	4.076	2.928	8053	1.193
5	52	5.213	2.318	7199	1.209
6	60	5.292	2.273	6050	1.203
7	68	5.339	2.249	5233	1.201
8	76	5.303	2.276	4556	1.207
9	84	5.519	2.172	4082	1.199
10	92	5.501	2.174	3685	1.196
11	100	5.700	2.113	3404	1.204
12	108	5.881	2.050	3085	1.206
13	116	6.078	2.003	2852	1.217
14	124	5.902	2.070	2654	1.222
15	132	5.852	2.085	2538	1.220
16	140	6.018	2.050	2493	1.234

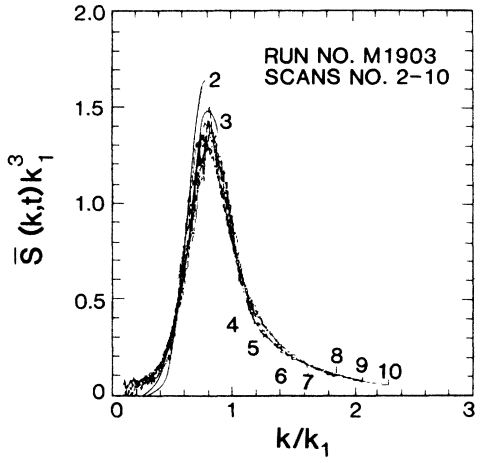

FIG. 12. Scaling plot of the normalized structure factor for the quench data shown in Figs. 9 and 10. The raw data for the first two photodiode array scans are replaced here by smooth lines so as not to obscure the scaling behavior of the later scans. Short vertical lines represent the upper limit of the data for each scan ($k = 8.5\times10^3$ cm^{-1}).

tively low signal-to-noise ratio, are replaced here by smooth lines. Also, scans 11–16, which deviate noticeably from the scaling function only where the substructure is well developed, are omitted for the sake of clarity. The only systematic differences in $F(k/k_1)$ observed from scan to scan are, first, a slight tendency for the earliest two scans to have a higher peak height (which could be due to the errors inherent in our extrapolation technique), and secondly, a tendency of each successive scan to fall below the preceding scans in the region $1.2 < k/k_1 < 1.8$. This latter effect is also noticeable in Fig. 13, where the scaling function is shown in log-log form. Here, the strong substructure in scans 11–14 manifest itself mainly through an increasing departure from

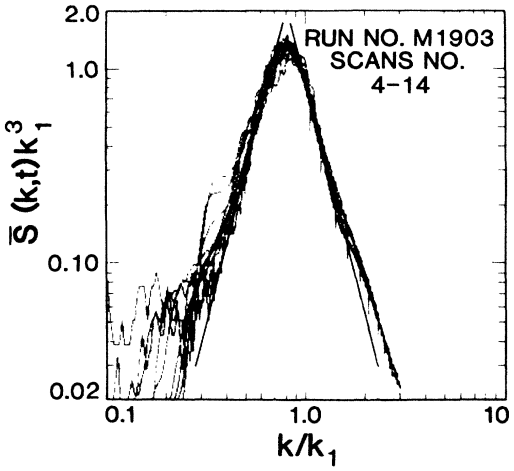

FIG. 13. Same data as in Fig. 12, but plotted in log-log form. The solid lines are drawn with slopes of 4 and −4. Noise in the data for earlier time scans at low k values, just visible in Fig. 12, is strongly amplified here. The data lying below the ordinate value of 0.10 should probably be neglected.

the scaling form in the region $0.3 < k/k_1 < 0.5$. The "hash" seen at the lowest k/k_1 values is due to noise in the earlier scans being strongly amplified by the scaling terms. The remarkable feature in this plot is the apparent symmetry of the shape function $F(k/k_1)$. Figure 13 suggest that, except for the immediate region of the main peak, $F(k/k_1)$ can be approximated by two simple equations:

$$F(k/k_1) = \begin{cases} A(k/k_1)^{\Phi} & \text{for } k/k_1 \leq 0.7 \\ A'(k/k_1)^{\Phi'} & \text{for } k/k_1 \geq 0.9, \end{cases}$$

with $\Phi \approx -\Phi' \approx 4$. The value $\Phi' = -4$ has been suggested on theoretical grounds by Furakawa.[36,37] Our data tend to confirm this value, as shown by the straight line with slope −4 in Fig. 13, but only if we ignore the data for values of F below approximately 0.15. This can be justified because errors due to background subtraction and due to analog-to-digital conversion are more significant at lower signal levels. From Fig. 12, one sees that only about 10% of our data points fall below this value. Likewise, the value $\Phi = 4$ is only justified for F values above 0.15, and then only if we ignore the substructure. Conversely, if we do not ignore our data below $F = 0.15$, then our best straight lines (by eye) through the data shown in Fig. 13 yield $\Phi' = 3.30 \pm 0.20$, and $\Phi = 3.20 \pm 0.30$. These latter values agree with all our data for all other quenches of the same type. Furthermore, the height of the main peak in $F(k/k_1)$, $F_m = 1.5 \pm 0.2$, is roughly independent of initial pressure and temperature over the same ranges we have investigated.

Thus, for quenches initiated from a homogeneous state, both the time dependence and the quench-depth dependence of $S(k,t)$ is reflected in the parameter $k_1(t)$. We have previously shown that the quench-depth dependence of the speed of the dynamical phase separation is in agreement with critical slowing-down phenomena.[17] Here we report on the $k_1(t)$ dependence for a single quench, i.e., for the same quench as shown in Figs. 9 and 10. Figure 14 shows k_1 versus t in log-log form, showing that the data can be well represented by Siggia's prediction[38] for relatively late-time behavior where hydrodynamic effects dominate the growth rate: $k_1 \propto t^{-1}$. Here, there is only a slight hint of a crossover from an earlier, diffusion-limited time behavior of slope $-\frac{1}{3}$, such as has been reported both by others[34,39] and by ourselves.[16] Factors responsible for this discrepancy include (1) the use of independent data in this study such as the onset of far-angle, low-level light scattering and/or the presence of a discernable "kink" in the $I_0(t)$ data to define the origin of time t_0; (2) the use of Lorentzian functions to extrapolate intensities for scans at early times; and (3) the use of a more sophisticated sample cell and a cyrogenic valve, which eliminates the anomalous afterheating observed with earlier sample cells. It appears that if there is indeed an earlier, slower growth rate of k_1^{-1}, then during that time period, the scattering light intensities are too weak to be sensed by our photodiode array.

The departure of the value of the moment S_2 from a constant allows us to follow the approximate paths of the evolving species in the X-T frame. We first normalize the

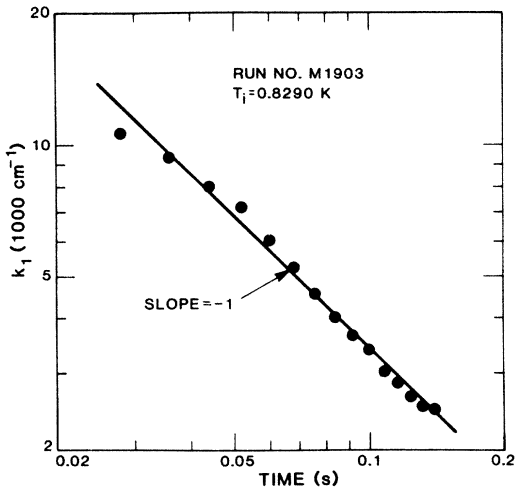

FIG. 14. Time dependence of the first moment of the data shown in Figs. 9 and 10. The origin of time was taken from the $I(0,t)$ data and was determined to occur 20 ms prior to the first recorded scan. This first scan showed no quench-induced scattering and was used for background subtraction; thus the first data scan is at 28 ms. In Ref. 20, the time origin was mistakenly given as 35 ms. A change in the time origin does affect the exponent of the evaluated time dependence of k_1, which explains the high value given in Ref. 20.

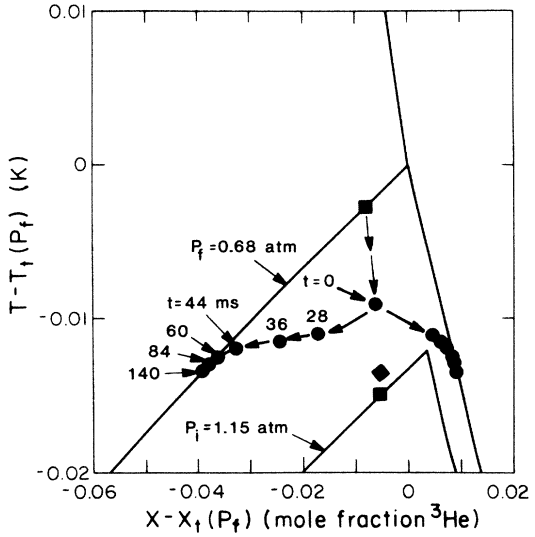

FIG. 15. The calculated paths of the decomposition states in quench M1903, plotted in the equivalent temperature-quench reference frame. The cloud point, as measured by the point labeled $t=0$, is anomalously low as discussed in Sec. V. Local phase separation is nearly complete after only three recorded time scans of angular scattering intensity. As discussed in the text, the system is no longer within the spinodal region at the time the first peak in scattering intensity is sensed by the photodiode array at $t=28$ ms.

S_2 values to the value of $(\Delta X)^2$ given by the equilibrium phase-separation lines at $t=\infty$, i.e., at the final equilibrium temperature T_f. This permits us to estimate ΔX for each scan of the quench. Our simultaneous measurements of $P(t)$ allow us to trace the path of the pressure quench in the equivalent temperature quench frame as shown in Fig. 15 (cf. Figs. 3 and 4). It should be pointed out that only ΔX can be calculated and not the individual concentrations of each evolving species, so that the placement of the data points in Fig. 15 is somewhat arbitrary. The quench proceeds initially along the line connecting the upper square symbol to the diamond symbol in Fig. 15. However, it is important to note that the quench never reaches the deep state represented by the diamond symbol. Instead, after reaching the cloud point, the two emerging new species follow paths directed toward the equilibrium phase-separation lines. The cloud point was detected 100 ms after the quench was begun or approximately 75 ms after the pressure started to fall as recorded by the CPG. The pressure at this instant ($t\equiv 0$) was 0.871 atm and the equivalent supercooling δT_m was calculated to be 6.3 mK. This supercooling is anomalously large and will be discussed in the next section. The photodiode array was activated 20 ms later, and the second scan, at $t=28$ ms, showed the first traces of a light scattering peak. Our analysis shows that by the end of the fourth scan, at $t=44$ ms, ΔX is nearly at the same value that is expected if the evolving species were at their equilibrium values for the instantaneous pressure. Thereafter, the phase-separation dynamics is rapid enough to permit ΔX to follow the exponential relaxation of the pressure to the final value P_f. By the end of the 16th scan the pressure has essentially reached P_f and phase separation on the local scale is essentially complete; but the minor-phase clusters are still ripening. At $t=0.9$ s, the end of the recording period, $I_0(t)$ is still falling, showing that global phase separation is still not complete. From other data taken under similar conditions using longer recording times, we estimate that $I_0(t)$ would start to recover at $t\sim 2$ sec, with bulk phase separation and equilibrium essentially complete at $t\sim 5$ sec.

B. Off-tricritical quenches

Because we have used only one composition of ^{3}He-^{4}He to make these measurements, off-critical quenches are necessarily those begun from already phase-separated states, as shown in Fig. 4. Several series of off-critical quenches were performed by first positioning the laser beam in the lower superfluid state of initially phase-separated mixtures and then quenching to ambient pressure. Two different types of paths were followed. First, as shown by the open circles in Fig. 16, we maintained the initial temperature constant and varied the initial pressure. In each subsequent quench, the pressure was reduced until no light scattering was observed following depressurization. Secondly, by keeping the initial pressure constant and lowering the initial temperature for each quench, we followed paths which parallel the final equilibrium superfluid coexistence boundary, as shown by the other sets of symbols in Fig. 16. Both procedures lead to the same qualitative observations, as discussed below. Beginning with initial states which were near X_t, we observed collapsing halos which were identical to those discussed in the preceding section. (In fact, the second solid square from the right in Fig. 16 represents quench M1903

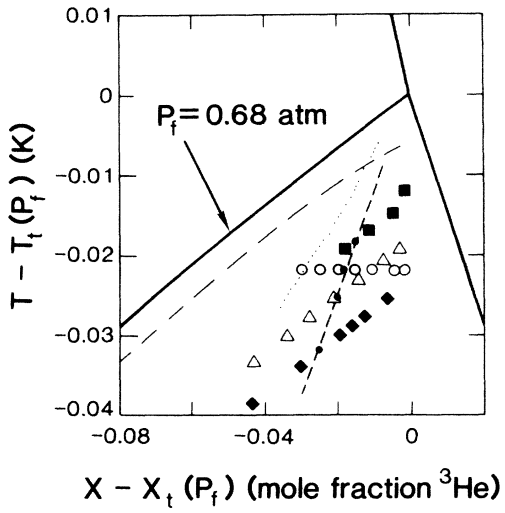

FIG. 16. Location of initial states for several series of off-tricritical quenches, relative to the final pressure P_f. The cloud line is shown here as a dot-dashed line. Dashed line connects points where an abrupt change in decomposition dynamics was noted. Estimations of decomposition paths for the quenches adjacent to the dashed line have enabled us to locate the left-hand spinodal boundary, shown as a dotted line. ■, series M19; ○, F26; △, series AP22; ◆, series F24.

that is discussed extensively in Sec. IV A.) As the initial composition was moved progressively farther from X_t, we continued to see well-defined halos that obeyed the scaling hypothesis. We also observed a faster speed of halo collapse, in agreement with the tricritical slowing-down phenomena which we have reported previously.[17] However, at initial compositions even farther from X_t, a new effect is observed. Halos, as such, are no longer observed; instead, the scattered light has a pattern of a large, nearly uniform disk that collapses while intensifying. The data no longer scale well, except, as shown in Fig. 17, for k values above $\sim 1.5k_1$, where the $F(k/k_1)$ data appear to follow the same $\Phi' = -4$ dependence as was observed for near-tricritical quenches. Also, the time dependence of the computed first moments k_1 continue to follow the form $d \ln k_1(t)/d \ln t = -1$.

Concurrent with this change in the pattern of the scattered light, a change in speed of the collapsing scattering pattern is observed. To quantify the collapse rate, we used the analytical procedure discussed in our tricritical slowing-down study,[17] and compare scattering-pattern collapse rates using the elapsed time $t_{k'}$ for the k_1 values of different quenches to reach a fixed value of k (taken here as $k' = 4000$ cm^{-1}). If the expected tricritical slowing-down behavior is obeyed, then the quantity $\epsilon t_{k'}$ should be a constant, where $\epsilon \equiv (T_t - T)/T_t$ is the reduced temperature of the quench. In order to intercompare the various series of off-critical quenches measured along different thermodynamic paths, these values are plotted against the tricritical scaling parameter $-Z \equiv \epsilon X_t / |X_t - X|$. Lines of constant Z are straight lines emanating from the relative tricritical point (0,0) in Fig. 16. Figure 18 shows the data for the constant temperature series of quenches (open circles in Fig. 16). At a Z value of ~ -0.96, there is an abrupt departure from the expected tricritical slowing-down behavior. The data for lower values of $-Z$ actually indicate just the opposite effect, i.e., the collapse rates slow down as we get farther away from the tricritical point, as can be seen in the data shown in Fig. 6. Similar plots for the constant-pressure series of quenches show very similar behavior, with an abrupt departure from $\epsilon t_{k'} = \text{const}$ at nearly the same value of Z. For the entire series of quenches, this departure value is $Z = -0.94 \pm 0.02$. We have plotted these departure points along each of the series paths as a small solid circle in Fig. 16. The straight dashed line drawn through these points, if extended, would intersect the tricritical point, as expected for a line of constant Z. To the right of this line we observe tricritical slowing-down and halo scattering patterns that obey scaling. But to the left of the dashed

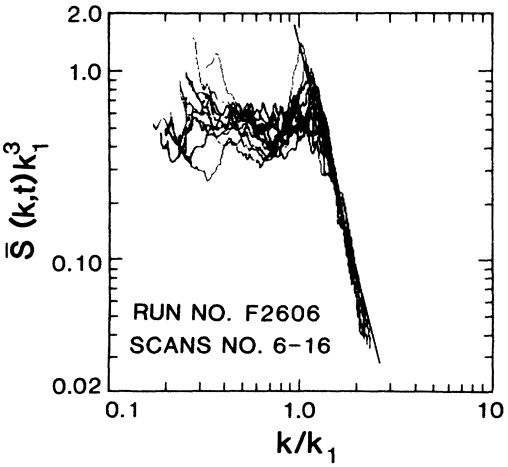

FIG. 17. Scaling plot of light scattering data for a quench which remains in the metastable region. The initial state is shown in Fig. 16 as the second circle from the left. Solid line through the data for $k/k_1 > 1.0$ is drawn with a slope of -4.

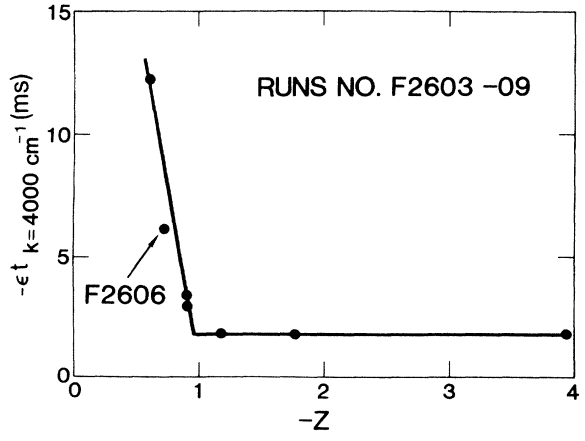

FIG. 18. Scaled decomposition rate as a function of the tricritical scaling parameter, for quench series F26. Tricritical slowing-down behavior is evident in the data for $-Z > 1$. The intersection of the two straight lines through the data defines a point on the dashed demarcation line shown in Fig. 16.

line, we observe "tricritical speeding up" and scattering patterns that are more disk-shaped and which obey the scaling hypothesis only partially. Figure 18 suggests that the demarcation between these two different types of dynamic phase separation is quite sharply defined. We are thus tempted to label the dashed line in Fig. 16 as the (left-hand) experimental spinodal line, separating the unstable, spinodal region on the right from the metastable region on the left where phase separation proceeds due to classical homogeneous nucleation.

However, if the data in Fig. 18 are to be interpreted by postulating the existence of a spinodal boundary, the actual boundary must lie to the left of the demarcation line shown in Fig. 16. This is because of the fact that the symbols in Fig. 16 represent the initial states for each quench, with reference to the initial pressure P_i, not the final pressure P_f. As is evident from Fig. 15, these deeply lying states are never achieved by the finite quench rates used here. However, we propose that for these quenches which lie to the right of the demarcation line in Fig. 18, the rate is sufficient to permit the system to "punch" into the spinodal region. We hypothesize that the system needs to be within the spinodal region only briefly, i.e., just long enough to establish a periodic array of minor phase clusters, in order for the ensuing decomposition and ripening stages to continue to follow spinodal decomposition dynamics for a considerable length of time. We also propose that for those quenches to the left of the demarcation, the spinodal is not reached and a periodic array of nucleation sites is not established. Therefore, somewhere along the left-hand decomposition path for the quenches to the right of the demarcation, the spinodal boundary is crossed. Also, for the quenches which lie to the left of the demarcation, the left-hand decomposition path does not cross the spinodal. Therefore we could set an approximate lower limit (in terms of concentration X) to the left-hand spinodal boundary if we could measure the largest $-Z$ value reached by the quenches which we do not follow spinodal decomposition. We cannot make an accurate analysis of the quench paths for these quenches, because the data do not scale well. Nonetheless, we can approximate the deepest penetration of the quench into the miscibility gap by evaluating the equivalent point in the P_f phase diagram where light scattering is first detected by the photodiode array. This procedure, employed for the quench in each series which lies just to the left of the demarcation line, has allowed us to crudely fix the position of the left-hand spinodal line, and this is shown in Fig. 16 as a dotted line.

Whether or not we have accurately located this spinodal line, we believe that the experimental evidence is strong that we are seeing the effects of a rather sharp spinodal boundary. First, the absence of disklike scattering patterns and the clean scaling behavior of halolike scattering patterns (for quenches which reach the spinodal boundary) are consistent with the expectations for spinodal decomposition. Second, for quenches which do not reach the spinodal region, the appearance of disklike scattering patterns is just what can be expected from homogeneous nucleation, as discussed in Sec. I; i.e., no periodic array of minor-phase sites is established and the stochastic effects of homogeneous nucleation dominate the dynamics.

Recalling from Fig. 5 that a disklike scattering pattern generally follows the appearance and collapse of a halo pattern, we conclude that the very late stages of decomposition or ripening proceed independently from the earlier spinodal behavior. In other words, after a sufficient time, the periodic "imprint" of minor-phase sites is lost to the system. These observations lead us to conclude that there is no evidence in the present data to support the conjecture of Binder[4] that diffusion-dominated ripening will lead to a more uniform distribution of major, growing clusters. However, the apparent scaling of the data for $k/k_1 > 1.5$ shown in Fig. 17 might indicate that the distribution of minor clusters is disappearing or shrinking according to a diffusion-limited rate law.

While we have not explicitly measured the light scattering amplitudes for the disks which appear following the collapse of halo patterns, there is some evidence in the wide-angle scattering measurements that these "disks" have a broad structure. The multiple peak of wide-angle scattering light shown in Fig. 7 can be tentatively interpreted as follows: At the faster quench rate, the system is brought into the spinodal region quickly and the first peak at 13° is the precursor to the halo which is later seen collapsing to small angles by the photodiode array. This first peak is quite smooth, suggesting that the spinodal region was reached before homogeneous nucleation in the metastable region had had sufficient time to promote a significant number of randomly oriented nucleation sites. At the slower quench rate, the first peak at 13° is noisy, suggesting that the system now has spent enough time in the metastable region to develop randomly oriented nucleation sites. Later, however, the spinodal region is reached, and a periodic array of minor-phase clusters is quickly established. The noise is therefore suppressed and a smooth halo pattern is observed later on the photodiode array. For both quenches, the subsequent ripening eventually becomes chaotic and an enlarging scattering disk emerges. Thus the rising side of the second peak observed at 13° for both quench rates may be the wide-angle tail of this disk. As the system ripens further, the smaller species in the distribution disappear and the scattering disk collapses, completing the formation of the second peak. The third peak in the wide-angle scattering intensity cannot be explained by this argument, but may be due to multiple scattering effects as the dispersions become more turbid.

The tricritical speeding up observed to the left of the spinodal is in qualitative agreement with the observations of Benda, *et al.*[21] Their data were taken at much wider intervals than the present series of quenches, but can be analyzed for speed of halo collapse at the same wave vector $k' = 4000\ \text{cm}^{-1} = 2.3°$. Reduced to the form $\epsilon t_{k'}$ versus $-Z$, their data are not inconsistent with the present findings and indicate that only their quench labeled A is within the tricritical slowing-down region, a conclusion consistent with our previous intercomparison.[17]

The inverse concentration susceptibility $(\partial\Delta/\partial X)_T$, also called the chemical potential gradient, is quite large along the phase-separation boundaries in ^{3}He-^{4}He mixtures,[40]

except at the tricritical point where it vanishes. The values are also quite asymmetric, being approximately ten times larger along the ^{3}He-rich phase boundary. This implies that theoretical estimations made by extrapolating free-energy isotherms to inside the miscibility gap should lead to more sharply defined spinodals, and especially, spinodals which are noticeably displaced toward the ^{3}He phase boundary. Using a phenomenological model of ^{3}He-^{4}He mixture dynamics,[41] Hohenberg and Nelson[42] have incorporated the data of Ref. 40 and predicted the positions of the spinodal lines. They do find strong asymmetry, with the left-hand spinodal defined "fuzzily" one-third of the way into the miscibility gap, i.e., $X_\sigma - X^- \simeq \frac{1}{3}(X^+ - X^-)$, where X^+ and X^- are the normal and superfluid coexistence boundaries, respectively, and X_σ is the left-hand spinodal line. They also predict a sharply defined right-hand spinodal, located very close to X^+. Our measurements place X_σ at approximately 42% of the distance across the miscibility gap, i.e., $X_\sigma - X^- = 0.42(X^+ - X^-)$. Considering the possible errors in the present estimation of the location of this spinodal line, and the error inherent to the linear model employed in Ref. 42, the agreement is remarkable.

A last comment on our measurements of spinodal decomposition is in order. Referring to Fig. 15, the first peak in scattered light detected by the photodiode array, occurring at $t = 28$ ms, lies outside the spinodal region as defined by the dotted line in Fig. 16. Therefore, to be accurate, we have made no quantitative measurements with our photodiode array while the decomposing system was actually inside the spinodal region. Again, we conclude that our data measure the dynamic behavior during the later stages of ripening, but add that the ripening is clearly affected by whether or not a periodic array of minor-phase sites (clusters) is first produced in the earlier spinodal decomposition stage.

V. HOMOGENEOUS NUCLEATION

A. Introduction

Liquid mixtures of ^{3}He and ^{4}He below the tricritical point T_t provide an excellent opportunity to study metastability and homogeneous nucleation in a quantum system. The amount of attainable supercooling of the homogeneous ^{3}He-^{4}He mixture in the metastable region of the miscibility gap and the lifetime of such supercooled states are measures of the degree of metastability of the system. Classical theories of nucleation, such as that of Becker and Döring (BD),[5,6] predict a kinetic limit to the supercooled metastable state where the lifetime of such states becomes infinitesimally small. Previous measurements of lifetimes of metastable states in liquid ^{3}He-^{4}He mixtures by Brubaker and Moldover[43] to determine the nucleation limit are at sharp variance with that expected from classical nucleation theory. Their experimental results suggest homogeneous nucleation limits of supercooling that are an order of magnitude smaller than that predicted by the classical theory. It should be mentioned that the validity of classical nucleation theory for a quantum system is not a question because it has been shown recently[44] that the BD theory does accurately predict the limit of metastability in liquid ^{4}He, a quantum liquid. The experiments of Brubaker and Moldover appear to be influenced by the walls of their sample cell and, consequently, their results might be attributed to *heterogeneous* nucleation.

Recently, Alpern *et al.*[13] found that at reduced temperatures $\epsilon = (T_t - T)/T_t > 0.03$, the maximum amount of supercooling δT_m was in good agreement with that expected from the classical nucleation theory as adapted to the critical region by Langer and Turski.[45] However, at temperatures closer to the tricritical point, the maximum supercooling tends to diverge from the classical theory prediction. Although such a divergence in supercooling near a critical point has been observed in organic binary mixtures,[8–12] Alpern *et al.*[13] suggested that the divergence is much stronger in the case of ^{3}He-^{4}He mixtures. They also point out that this feature of stronger divergence of supercooling near T_t could be a peculiarity of tricritical systems.

The divergence of supercooling as $\epsilon \to 0$ is an anomalous behavior since it is not predicted by the classical nucleation theory. However, such anomalous supercooling can be explained in terms of critical slowing down of diffusion processes as first described by Binder and Stauffer[46] and later in more detail by Langer and Schwartz.[47] Experimentally, one typically determines the limit of supercooling by cooling slowly into the metastable region while monitoring the turbidity of the system. The cloud point following homogeneous nucleation is, therefore, measured only after the evolving minority-phase clusters or droplets have grown large enough (of the order of 1000 Å) to begin to scatter visible light strongly. Consequently, the cloud-point phenomenon always lags in time behind the actual onset of homogeneous nucleation. Because of critical slowing down, this time lag gets progressively longer as one approaches the critical point. Coupled with the finite quench rates used in actual experiments, this appears to indicate additional supercooling. Recently, Rabin and Gitterman[48,49] have proposed a quench-rate-dependent time lag that is associated with the establishment of a steady-state regime of nucleation following the quench. They show that for a "fast" quench, the time of decay of a metastable state increases substantially near the critical point. Furukawa[50] has similarly proposed a waiting time for the nucleation reaction in terms of a transient effect of the droplet-formation barrier to explain the anomalous supercooling observed in experiments near the critical point. Both Rabin and Gitterman, and Furukawa have essentially proposed mechanisms for the enhancement in the stability of the metastable region near the critical point. According to their theories, the anomalous supercooling is explained in terms of the enhanced stability of the metastable state coupled with the finite quench rates. In other words, the measured cloud point is equivalent to the point where the nucleation reaction *starts*. It may be difficult to experimentally show which explanation of the could-point is more appropriate. However, it is obvious that all the above mechanisms indicate that the cloud-point phenomenon should depend on the quench rate. In this section, we present our measurements of the cloud point in ^{3}He-^{4}He mixtures near the tricritical point and show the effects of quench rate on the

measurements. A brief account of this experiment has been published previously.[51]

B. Experimental

Supercooling in the ^{3}He-^{4}He liquid mixture of tricritical composition also was produced by the pressure-quench technique. Figure 19 shows a typical pressure-quench history. The cloud point is indicated by the arrow where I_0 suddenly starts to decrease. The actual supercooling δT_m was determined from the pressure P_{CP} at the cloud point, the known pressure dependence of the tricritical temperature $T_t(P)$,[30] and the slight rise in temperature dT that accompanies the pressure quench. Figure 20 shows the phase diagram of ^{3}He-^{4}He at the initial pressure P_i and at the pressure P_{CP} when the cloud point is observed. $T_t(P_i)$ and $T_t(P_{CP})$ are the respective tricritical temperatures corresponding to these two pressures. The relevant quantities δT_m, ΔT, and dT are given by

$$\delta T_m = T_{PS} - T_{CP} , \tag{10a}$$

$$\Delta T = T_t(P_{CP}) - T_{PS} , \tag{10b}$$

and

$$dT = T_{CP} - T_i = 0.0028(P_i - P_{CP}) , \tag{10c}$$

from Eq. (2). In Eq. (10a), T_{PS} is the equilibrium temperature of the ^{4}He-rich phase of the phase-separated mixture at pressure P_{CP} and T_{CP} is the instantaneous temperature at the moment that the cloud point is observed.

Our pressure-quench experiment is equivalent to the usual temperature-quench experiments although the paths are different. For example, in our case the starting point is at (T_i, X_i), which describes the temperature T_i of the initially phase-separated mixture (^{4}He-rich phase) at concentration X_i corresponding to the phase diagram of initial pressure P_i. Following the pressure quench, this point

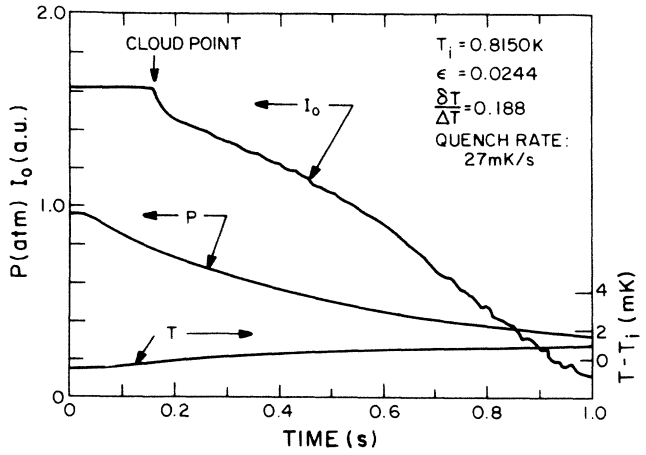

FIG. 19. Simultaneous measurements of pressure, temperature, and forward transmission intensity I_0, during a pressure-induced quench into the miscibility gap. The sudden drop in I_0 is the signature of the cloud point.

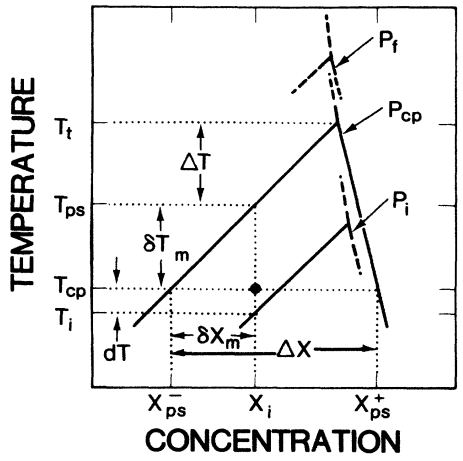

FIG. 20. Relevant supercooling and supersaturation quantities, defined in relation to the phase diagram for the instantaneous pressure P_{CP} when cloud-point phenomena are first observed.

moves up to (T_{CP}, X_i) because of the adiabatic heating dT. In comparison, in a temperature-quench experiment, the equivalent starting point would be T_{PS} on the phase-separation line belonging to P_{CP} and the corresponding cloud point would be reached by lowering the temperature to T_{CP}. Both type of experiments have the phase diagram at pressure P_{CP} in common. Therefore, for the purpose of comparing our data with others who have used temperature quenches, we define $\epsilon' = \Delta T / T_t(P_{CP})$ as the reduced temperature at the starting point where ΔT is given by Eq. (10b). We should point out that although the expressions for δT_m and ΔT as given by Eqs. (10a) and (10b) are correct, they cannot be directly used to evaluate these quantities because the temperatures T_{PS} and T_{CP} are not measured. However, δT_m and ΔT can be determined easily from the knowledge of P_{CP}, T_i [hence $T_t(P_{CP})$ and $T_t(P_i)$], and dT, all of which are measured; the known pressure dependence of the tricritical temperature $T_t(P)$;[30] the shape of the coexistence curve near the tricritical point;[52] and the fact that shape of the coexistence curve near T_t is invariant under pressure.[53] From simple geometry and the values $dT_t/dX = -3.29$ K/mole and $dT_{PS}/dX = 0.312$ K/mole which, respectively, describe the variations of the tricritical temperature T_t and the ^{4}He-rich side of the coexistence curve T_{PS}^- as functions of composition for the pressure ranges used here, we have derived the following expressions that relate δT_m and ΔT to measured quantities:

$$\delta T_m = 1.095[T_t(P_{CP}) - T_t(P_i)] - dT , \tag{11a}$$

$$\Delta T = [T_t(P_i) - T_i] - 0.095[T_t(P_{CP}) - T_t(P_i)] . \tag{11b}$$

The supersaturation that corresponds to the supercooling δT_m is given by δX_m (see Fig. 20). The reduced supersaturation $y = \delta X_m / \Delta X$ near the tricritical point $T_t(P_{CP})$ can be approximated in terms of δT_m and ΔT from the triangular shape of the phase diagram as

$$y = 0.818 \delta T_m / (\delta T_m + \Delta T) , \tag{12}$$

in the range of interest.

C. Results and discussion

Three different rates of supercooling were used: 80, 21, and 13 mK/s. These are the average values of the cooling rates, determined from the $P(t)$ data, at the moment the light intensity I_0 begins to decrease (see Fig. 19). We found that the transmitted light intensity did not change appreciably in the normal upper phase following nucleation and it was somewhat difficult to determine the cloud point accurately. Because of the convenience in determining the cloud point with greater accuracy we performed all our measurements in the lower superfluid phase. Even in the superfluid phase, at reduced temperatures less than 0.001, it was difficult to determine accurately the location of the cloud point. There are two main reasons for this. First, very close to the tricritical point, the difference in the refractive index between the minority and the majority phase during initial stages of phase separation is so small that very little light is scattered and consequently, the transmitted light does not show much change. Secondly, because of critical slowing down, the droplet growth rates are very small and the phase separation proceeds at a much reduced rate, resulting in a very gradual change in the transmitted light intensity I_0. The horizontal part of I_0 preceding the cloud point indicates the time the mixture can remain metastable. For the slowest quench rate used (13 mK/s), this lifetime of the metastable state can be as long as one second. Much longer lifetimes are possible for quench rates slower than 13 mK/s and also when the difference between P_i and P_{CP} is small.

Figure 21 shows the reduced supercooling $\delta T_m/\Delta T$ as a function of ϵ' on a log-log plot for three different quench rates represented by the three different symbols. The crosses represent data in the superfluid phase of a ^{3}He-^{4}He mixture from Alpern *et al.*[13] for quench rates greater than 150 mK/s. These data have been corrected to conform to the definition for δT_m and ΔT given by Eqs. (10) and (11). The dashed line is the data from Strey *et al.*[54] for a quench rate of 30 mK/s in a lutidene-water mixture. The dotted line shows the data from Schwartz *et al.*[11] also for lutidene-water but for effective quench rates of less than 1 mK/s. The dot-dashed line represents predictions from classical nucleation theory. For values of $\epsilon' < 0.02$ the present data can be fairly well represented by straight lines and were fitted to the simple form $\delta T_m/\Delta T = a\epsilon'^b$. The values of the parameters a and b are given in Table II for the three quench rates. The dependence of maximum supercooling on the quench rate is obvious from Fig. 21. At $\epsilon' > 0.012$, the quench-rate dependence diminishes and the $\delta T_m/\Delta T$ data become consistent with the prediction from classical nucleation theory (dot-dashed line). Similar behavior was observed by Strey *et al.*[54] in a lutidene-water mixture for three different quench rates (see Fig. 8 of Ref. 54). Considering the different experimental techniques used (pressure quench versus temperature quench) and the disparate thermodynamic properties of the two systems, no meaningful inconsistency can be inferred from data in organic mixtures in comparison to either our data or those of Alpern *et al.*[13] in ^{3}He-^{4}He. In other words, there is no unreasonably stronger divergence in the ^{3}He-^{4}He supercooling data as $\epsilon' \to 0$. However, the effects of the particular experimental techniques used, such as pressure quench versus temperature quench, in determining the cloud point, have not been adequately studied. For instance, in temperature-quench experiments it is possible that heterogeneous nucleation begins at the walls of the sample chamber before the actual cloud point in the bulk of the sample is reached. In comparison, in pressure-quench studies such as ours, temperature gradients do not develop and the system is more conducive to observing homogeneous nucleation. It is not obvious at this point why there seems to be a quantitative disagreement between the present data and that of Alpern *et al.*[13] It is, however, not improbable that in the case of Alpern *et al.*, who did not use a completely closed cell and did not have an *in situ* pressure gauge, the actual quench rate in the system may be lower than that measured externally. Moreover, the inherent turbulence following a quench in the sample in their case may have affected the cloud-point measurements.

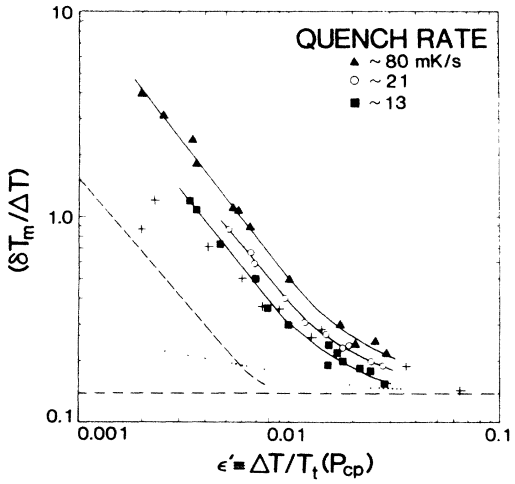

FIG. 21. Reduced supercooling vs the reduced temperature at the phase boundary for three different quench rates in the superfluid phase of a ^{3}He-^{4}He mixture. See text for an explanation of the data from other sources.

Although we do not find any meaningful difference in the divergence of supercooling between ^{3}He-^{4}He and organic binary mixtures, a difference can be expected for supersaturations on the basis of Furukawa's recent theory.[50] Furukawa has explained the anomalous supercooling in terms of a transient effect on the droplet formation barrier as discussed earlier. He describes the locus of the cloud point as

TABLE II. Experimental parameters for anomalous supercooling.

Quench rate (mK/s)	a	b
80	1.218×10^{-3}	-1.3107
21	1.217×10^{-3}	-1.2491
13	0.820×10^{-3}	-1.2784

$$y \propto \epsilon^{-\phi} \tau^{-3/8} , \tag{13}$$

where $y = \delta X_m / \Delta X$ is the reduced supersaturation (see Fig. 20), and τ is the characteristic observation time after a quench. The constant ϕ depends on the static critical exponents and is given by

$$\phi = \beta/2 + \gamma/4 + 3\nu/8 , \tag{14}$$

where β, γ, and ν have their usual meaning. In the case of ^{3}He-^{4}He mixtures, $\beta = \gamma = \nu = 1$, and therefore the value of $\phi \simeq 1.125$; whereas $\phi \simeq 0.70$ for organic mixtures. This suggests a stronger divergence of y for ^{3}He-^{4}He as compared to the organic liquids. Figure 22 shows the same data as shown previously in Fig. 21 but in terms of reduced supersaturation y as a function of ϵ on a log-log plot. Here, in contrast to the usage in the earlier part of this section and in Fig. 21, ϵ is the reduced temperature at the point of maximum supercooling: $\epsilon = (\Delta T + \delta T_m)/T_t(P_{CP})$. In Fig. 22, the three straight lines are the best lines that can be drawn through the data points for each quench rate having a slope of -1.125. Although the agreement is rather qualitative, the data do not seem inconsistent with Eqs. (13) and (14). The quench-rate dependence of the supersaturation data is obvious. Each quench rate is expected to have a different observation time τ associated with it and thus the results of Fig. 22 are consistent with Eq. (13).

The dashed curve in Fig. 22 represents the supersaturation as a function of the reduced temperature for a completion time of 0.5 s (arbitrarily chosen) as predicted by Langer and Schwartz.[47] This completion curve has been derived from the plot of y_1 against $\log_{10}\tau_c$ in Fig. 8 of Ref. 47. Although the completion time is of the same order of magnitude as can be expected from the quench rates used in the experiment, the shape of the curve does not qualitatively agree with the data. Selecting other completion times within ± 0.1 s of 0.5 s, the curves fall beyond the range of the experimental data. Although we have drawn straight lines through the data with a fixed slope of -1.125 for comparison with Furukawa's theory, it is obvious that the actual data can be represented better by curves than the straight lines. Although the predicted value of $\phi \simeq 0.7$ [Eq. (14)] for organic mixtures, the measured values[11] fall in the range between 0.5—1.0. Thus, it can be concluded from the data presented here that there is no meaningful difference in the divergence of relative supercooling or supersaturation between ^{3}He-^{4}He and organic mixtures. In other words, the dynamics of a first-order phase transition in a quantum and tricritical system such as ^{3}He-^{4}He appears to be the same as that observed in normal systems such as organic mixtures.

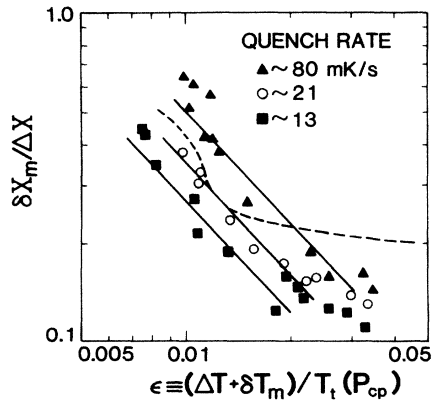

FIG. 22. Reduced supersaturation vs reduced temperature for the data presented in Fig. 21. Straight lines through the data for each quench rate are drawn with a slope of -1.125. Dashed line is a prediction from Ref. 47 based on a "completion time" of 0.5 s.

VI. OTHER OBSERVATIONS

We would be remiss not to mention some of the interesting phenomena which we observed during the course of our measurements. Most of these observations were made using the laser shadow technique described in Sec. II.

A. Gravitationally induced optical effects

We typically confirmed the composition of our ^{3}He-^{4}He mixtures by several means, the simplest of which was to slowly cool the sample and to note the temperature at which a phase-separation interface could be first detected. This technique worked well for mixtures with an overall composition greater than X_t. However, when the ^{3}He mole fraction was less than X_t, large discrepancies were observed. Specifically, we observed the appearance of an interface at temperatures as high as 20 mK above T_t, where phase separation is thermodynamically forbidden

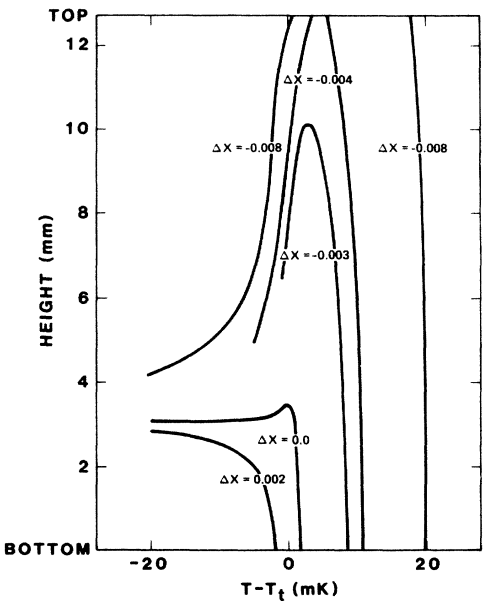

FIG. 23. Positions of the visible interface between ^{3}He-rich and ^{4}He-rich phases as a function of temperature, calculated for several compositions near the tricritical value. Gravitationally induced concentration gradients lead to the appearance of visible interfaces at temperatures above the tricritical value along the λ line.

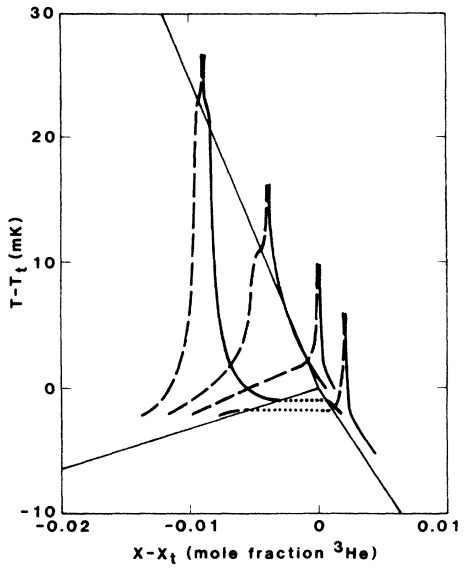

FIG. 24. Spread in concentration due to gravitationally induced gradients over the height of our sample cell, calculated for several values of overall composition near the tricritical value. For each composition, the solid curve represents the concentration at the top of our cell, while the dashed line represents the concentration at the bottom. Dotted lines represent discontinuities in concentration occurring at the equilibrium phase-separation boundaries.

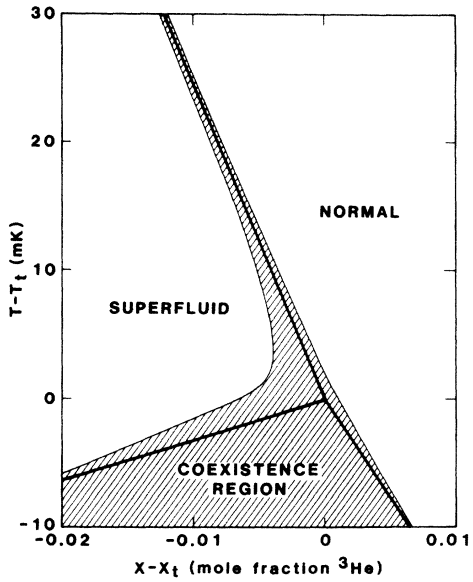

FIG. 25. The effective phase diagram for ^{3}He-^{4}He mixtures in a cell of height 1.27 cm. Gravitational effects broaden the miscibility gap and raise it to include the λ line. Only below the equilibrium coexistence boundaries will one have a true discontinuity in composition due to first-order phase separation. However, within the shaded area, an interface between coexisting superfluid and normal phase will be present, although this interface is more difficult to observe as one moves to higher temperatures along the λ line.

under equilibrium conditions. The movement of this interface with further cooling was quite puzzling; after first appearing at the bottom of the sample cell, it moved rapidly upwards and then moved downwards again. For a range of relative concentrations (induced by initial pressures greater than SVP), the interface disappeared completely out of the top before reappearing, while the cell was cooled slowly toward T_t from above. In a previous publication,[55] it was shown that these effects are due to the gravitationally induced concentration gradient $(\partial X/\partial z)_T$ present in systems near a critical point, being especially strong in ^{3}He-^{4}He liquid mixtures. In Ref. 55, tricritical scaling[56] was invoked to calculate the concentration gradients, and it was shown that the λ line caused a kink in $(\partial X/\partial z)_T$ which leads to a visible interface when illuminated by uniform, horizontally oriented, laser light. Our observations were quite well explained by this analysis, as shown in Fig. 23 where we plot the calculated positions of the interface as a function of temperature relative to T_t for several values of overall concentrations.

In Fig. 24, we show the calculated spread in concentration over the 1.27-cm height of our sample cell for the same values of X as shown in Fig. 23. The effects are clearly the strongest for values of X just below X_t. Near the λ line, the behavior shown here may be compared with qualitative estimations of gravitationally induced concentration spreading shown in the work of Gearhart and Zimmerman.[57] Such data have allowed us to construct the effective phase diagram for our cell in a gravitational field of 1g, shown in Fig. 25. It is obvious that gravity widens the coexistence region and extends it to higher temperatures along the λ line.

B. Interface splitting

Because we routinely observed each quench visually using the laser shadow technique before proceeding with light scattering measurements, we noted a strange phenomenon when pressurizing phase-separated mixtures to higher pressures. Referring to Fig. 4, we note that while increasing the pressure from 0.65 to 1.65 atm, we expect the interface, initially present near the bottom of the cell, to move upwards to near the middle of the cell. However, what we always observed was that, as soon as the pressure was increased, the initial interface split into two interfaces. One interface would strengthen in intensity and move upwards, eventually settling at the expected midpoint of the cell, while the other interface would remain stationary, gradually weakening in intensity until it no longer was visible. This effect is no doubt also a consequence of the gravitationally induced concentration gradients in the mixtures, but we find it difficult to explain quantitatively. It appears that equilibration of the mixture following a gradual increase in pressure occurs globally throughout the mixture, not just by a relative flow of mixture components across the superfluid-normal interface.

C. Spontaneous droplet formation at low temperatures

We once cooled our (tricritical) mixture to 0.507 K, in preparation for searching for halo patterns in the scat-

tered laser light. However, at the SVP (no ^{4}He in the pressurization bellows) we observed a flickering in the forward intensity $I(0,t)$. Upon expanding the laser beam, we observed the formation of droplets in the lower phase in the shadow image. These droplets could also be observed directly in the cell with the expanded laser beam as backlighting. The droplets would "spring" upwards from random locations in the lower phase and disappear upon striking the normal-superfluid interface. The droplets were therefore ^{3}He-rich normal droplets,[16] forming spontaneously in the lower superfluid phase. However, we have no explanation as to why the lower phase should be supersaturated with ^{3}He. ^{4}He film flow upwards along the walls of the cell could create such a condition, but we expect any temperature gradient in the cell to be in the opposite direction, i.e., the ^{3}He pot is thermally attached to the top of the sample cell. This "reverse fountain effect" remains unexplained.

D. Multiple interfaces

Upon completing a series of measurements, we usually added heat to the ^{3}He pot to evaporate the remaining ^{3}He coolant. As the sample cell warmed, we observed the formation of multiple interfaces in the shadow image. There were often as many as seven regularly spaced interfaces which persisted until the sample cell temperature reached approximately 1 K. We interpret these interfaces as the divisions between convection cells, caused by the Rayleigh-Bénard instability in ^{3}He-^{4}He mixtures when heated from above.

ACKNOWLEDGMENTS

We would like to thank W. E. Keller for his continued interest and support for this work. We have benefited from discussions with J. L. Lebowitz, J. S. Langer, W. I. Goldburg, J. D. Gunton, J. C. Wheatley, and L. J. Campbell during the course of this work. Special thanks are due to A. Isensee and J. Dyson, who built the sample cells, and to T. Geelan and C. Espinoza for technical assistance with the apparatus. This work was supported by the U.S. Department of Energy. In the early stages of this work, we received partial support from the U.S. National Aeronautics and Space Administration Working Group for Physics and Chemistry in Space (NASA-PACE).

[1]For a recent review, see J. D. Gunton, M. San Miguel, and P. S. Sahni, in *Phase Transitions and Critical Phenomena,* edited by C. Domb and J. L. Lebowitz (Academic, London, 1983), Vol. 8.

[2]J. S. Langer, Physica **73**, 61 (1974).

[3]A. Sur, J. L. Lebowitz, J. Marro, and M. H. Kalos, Phys. Rev. B **15**, 3014 (1977).

[4]K. Binder, Phys. Rev. A **29**, 341 (1984), and references therein.

[5]R. Becker and W. Döring, Ann. Phys. (Leipzig) **24**, 719 (1935).

[6]See, for example, J. Frenkel, *Kinetic Theory of Liquids* (Dover, New York, 1955); *Nucleation,* edited by A. C. Zettlemoyer (Dekker, New York, 1969); *Nucleation Phenomena,* edited by A. C. Zettlemoyer (Elsevier, New York, 1977).

[7]I. M. Lifshitz and V. V. Slyozov, J. Phys. Chem. Solids **19**, 35 (1961).

[8]B. E. Sundquist and R. A. Oriani, J. Chem. Phys. **36**, 2604 (1962).

[9]R. B. Heady and J. W. Cahn, J. Chem. Phys. **58**, 896 (1973).

[10]J. S. Huang, W. I. Goldburg, and M. R. Moldover, Phys. Rev. Lett. **34**, 639 (1975).

[11]A. J. Schwartz, S. Krishnamurty, and W. I. Goldburg, Phys. Rev. A **21**, 1331 (1980).

[12]Rebekah G. Howland, Ning-Chih Wong, and Charles M. Knobler, J. Chem. Phys. **73**, 522 (1980).

[13]P. Alpern, Th. Benda, and P. Leiderer, Phys. Rev. Lett. **49**, 1267 (1982).

[14]J. S. Langer, M. Bar-on, and H. D. Miller, Phys. Rev. A **11**, 1417 (1975).

[15]For a recent review, see Walter I. Goldburg, in *Scattering Techniques Applied to Supramolecular and Nonequilibrium Systems,* edited by S. M. Chen, B. Chu, and R. Nossal (Plenum, New York, 1981), p. 383.

[16]J. K. Hoffer, L. J. Campbell, and R. J. Bartlett, Phys. Rev. Lett. **45**, 912 (1980).

[17]Dipen N. Sinha and James K. Hoffer, Phys. Rev. Lett. **50**, 515 (1983).

[18]Dipen N. Sinha and James K. Hoffer, Physica **107B**, 155 (1981).

[19]Dipen N. Sinha and James K. Hoffer, Rev. Sci. Instrum. **55**, 875 (1984).

[20]James K. Hoffer and Dipen N. Sinha, in *Proceedings of the 17th International Conference on Low Temperature Physics,* edited by U. Eckern, A. Schmidt, W. Weber, and H. Wuhl (Elsevier, Amsterdam, 1984), Pt. II, p. 961.

[21]Th. Benda, P. Alpern, and P. Leiderer, Physica **107B**, 157 (1981).

[22]Th. Benda, P. Alpern, and P. Leiderer, Phys. Rev. B **26**, 1450 (1982).

[23]J. Marro, J. L. Lebowitz, and M. H. Kalos, Phys. Rev. Lett. **43**, 282 (1979).

[24]*The Superalloys,* edited by C. T. Sims and W. C. Hagel (Wiley, New York, 1972).

[25]S. Krishnamurthy and W. I. Goldburg, Phys. Rev. A **22**, 2147 (1980).

[26]Paramdeep S. Sahni and J. D. Gunton, Phys. Rev. Lett. **45**, 369 (1980).

[27]D. Beysens and F. Perot, J. Phys. (Paris) Lett. **45**, L31 (1984).

[28]Tatsuhiro Imaeda, Akira Onuki, and Kyozi Kawasaki, Prog. Theor. Phys. **71**, 16 (1984).

[29]J. del Cueto, R. L. Johnson, T. Rhode, F. H. Wirth, and E. H. Graf, J. Phys. (Paris) Colloq. **41**, C7-133 (1980).

[30]P. Leiderer (private communication).

[31]P. Alpern, Th. Benda, and P. Leiderer, in *75th Jubilee Conference on Helium-4,* edited by J. G. M. Armitage (World Scientific, Singapore, 1983), p. 144.

[32]A. Craievich and J. M. Sanchez, Phys. Rev. Lett. **47**, 1308 (1981).

[33]W. I. Goldberg, C.-H. Shaw, J. S. Huang, and M. S. Pilant, J. Chem. Phys. **68**, 484 (1978).

[34]Y. C. Chou and W. I. Goldberg, Phys. Rev. A **20**, 2105 (1979).

[35]Y. C. Chou and W. I. Goldberg, Phys. Rev. A **23**, 858 (1981).

[36]H. Furukawa, Phys. Rev. Lett. **43**, 136 (1979).

[37]H. Furukawa, Phys. Rev. A **23**, 1535 (1981).

[38]E. D. Siggia, Phys. Rev. A **20**, 595 (1979).

[39]N.-C. Wong and C. M. Knobler, J. Chem. Phys. **66**, 4707 (1977); **69**, 725 (1978).
[40]G. Goellner, R. Behringer, and H. Meyer, J. Low Temp. Phys. **13**, 113 (1973).
[41]E. D. Siggia and D. R. Nelson, Phys. Rev. B **15**, 1427 (1977).
[42]P. C. Hohenberg and D. R. Nelson, Phys. Rev. B **20**, 2665.
[43]N. R. Brubaker and M. R. Moldover, in *Proceedings of the 13th International Conference on Low Temperature Physics,* edited by W. J. O'Sullivan, K. D. Timmerhaus, and E. F. Hammel (Plenum, New York, 1973), Vol. I, p. 612.
[44]Dipen N. Sinha, J. S. Semura, and L. C. Brodie, Phys. Rev. A **26**, 1048 (1982); **31**, 1957 (1985).
[45]J. S. Langer and L. A. Turski, Phys. Rev. A **8**, 3230 (1973).
[46]K. Binder and D. Stauffer, Adv. Phys. **25**, 343 (1973).
[47]J. S. Langer and A. J. Schwartz, Phys. Rev. A **21**, 948 (1980).
[48]Y. Rabin and M. Gitterman, Phys. Rev. A **29**, 1496 (1984).
[49]M. Gitterman and Y. Rabin, J. Chem. Phys. **80**, 2234 (1984).
[50]H. Furukawa, Phys. Rev. A **28**, 1729 (1983).
[51]Dipen N. Sinha and James K. Hoffer, in *Proceeding of the 17th International Conference on Low Temperature Physics,* edited by U. Eckern, A. Schmidt, W. Weber, and H. Wuhl (Elsevier, Amsterdam, 1984), Pt. II, p. 959.
[52]H. Kierstead, J. Low Temp. Phys. **35**, 25 (1979).
[53]P. Leiderer and W. Bosch, Phys. Rev. Lett. **45**, 727 (1980).
[54]R. Strey, J. Wagner, and D. Woermann, Ber. Bunsenges. Phys. Chem. **86**, 306 (1982).
[55]Shoou-Shinn Shiah and James K. Hoffer, in *Proceedings of the 17th International Conference on Low Temperature Physics,* edited by U. Eckern, A. Schmidt, W. Weber, and H. Wuhl (Elsevier, Amsterdam, 1984), Pt. II, p. 963.
[56]E. K. Ridel, H. Meyer, and R. P. Behringer, J. Low Temp. Phys. **22**, 369 (1976).
[57]G. A. Gearhart, Jr., and W. Zimmerman, Jr., Phys. Rev. B **19**, 2677 (1979), Fig. 7.

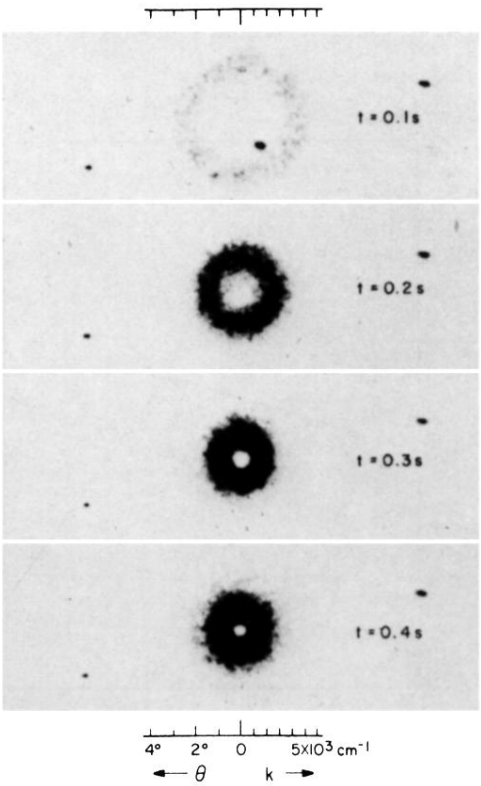

FIG. 5. Halo patterns in the light scattered by a liquid binary mixture of ^{3}He-^{4}He, following a pressure quench from 1.36 atm to the SVP at a temperature of 0.83 K. The mixture is of tricritical composition relative to the SVP phase diagram. The rate of decompression was approximately 0.68 atm/s during the events shown here. These are selected frames from cinematography shot at 50 frames/s, of the image formed by the scattered light on a viewing screen. The primary laser beam is allowed to pass through a 7-mm-diam hole, just visible only in the frame at 0.4 s. The three stationary black dots are the result of reflections of the primary beam from any of the ten optical windows along the light path in our cryostat.